journal of the international meteor organization

WGN

51:6
december 2023

Announcement International Meteor Conference 2024
Meteor spectroscopy: visual lookup for elements
2022 August Delta Capricornids
Comparison of three different camera systems

ISSN 1016-3115

WGN Vol. 51, No. 6, December 2023, pp. 143 – 174

Conferences

Ongoing meteor work

Front cover photo

This bright Geminid fireball was captured passing through Orion at $22^{h}00^{m}$ IRST ($18^{h}30^{m}$ UT) on 2022 December 14, from Shahrud, Semnan Province, Iran. Image courtesy: Amin Golesorkh.

Back over photo

Visualization of the first million orbits obtained by the Global Meteor Network. Radiant densites are plotted with a logarithmic color scale. Image courtesy: Tammo Jan Dijkema, CC-BY 4.0 Global Meteor Network.

Writing for WGN

This Journal welcomes papers submitted for publication. All papers are reviewed for scientific content, and edited for English and style. Instructions for authors can be found in WGN **45:1**, 1–5, and at `http://www.imo.net/docs/writingforwgn.pdf` .

Legal address

International Meteor Organization, Jozef Mattheessensstraat 60, 2540 Hove, Belgium.

Conferences

IMC 2024 in Kutná Hora, Czech Republic

Pavel Koten[1] *and Tomáš Henych*[1]

While the last IMC took place in a place of technological marvels of the present and future, for this year we would like to offer you a glimpse into our history. The conference will be held in a beautiful historic town that became famous for its silver mining in the Middle Ages and was one of the richest cities of its time. It still retains this fame today thanks to its inscription on the UNESCO World Heritage List.

1 Introduction

The next IMC will be held in Hotel Mědínek in Kutná Hora in the Czech Republic from 19th to 22nd September 2024. It will follow the Europlanet Science Congress in Berlin from 8th to 14th September. The date may be of interest to participants of this Congress, especially non-Europeans, who may wish to extend their stay in Central Europe and attend both meetings.

Figure 1 – Kutná Hora town panorama. Photo credit: Hotel Mědínek.

2 Conference venue

The conference will take you directly to the historic centre of the town, where the Hotel Mědínek Old Town*** is located in. All necessary technical equipment for the conferences is available here. It has a conference hall with a capacity of up to 120 seats. There is a coffee break room next to the hall. Two small lounges with 20 and 30 seats are also available. Free wi-fi is available throughout the hotel. Depending on their number, posters can be arranged along the walls of the conference hall or in one of the small lounges.

The hotel can accommodate up to 112 guests in 52 rooms. There are single, double, triple, and quadruple rooms. Each room has its own bathroom with toilet. The rooms are situated on three floors. A lift is available. Twelve rooms on the upper floor have a balcony.

[1] Astronomical Institute of Czech Academy of Sciences, Fričova 298, Ondřejov, 251 65, Czech Republic
Email: koten@asu.cas.cz

IMO bibcode WGN-516-koten-imc2024 NASA-ADS bibcode 2023JIMO...51..143K

Figure 2 – The conference hall can accommodate up to 120 seats in the theatre configuration. Photo credit: Hotel Mědínek.

Figure 3 – A double room. Photo credit: Hotel Mědínek.

The hotel restaurant has a capacity of 80 seats, and another 50 seats are available in the café next to the bar. The bar will be open until midnight. The café area will be available for continued discussions even after the closing hours of the bar.

Reception is open 24 hours a day. The hotel accepts cash (Czech koruna) and credit cards. There is an ATM nearby. A limited number of parking places are available in the courtyard and on the street in front of the building (25 in total, free of charge). More places are offered at a nearby partner car park (paid). The hotel offers a private wellness area with sauna, infra sauna, and whirlpool as well as a wide range of professional massages. For those who prefer to arrange their own accommodation, there are a number of other hotels in the vicinity of Hotel Mědínek.

Figure 4 – Café in front of the bar. Photo credit: H. Zichová.

3 Location

Kutná Hora is one of the most historically important towns in the Czech Republic. Its history began to be written in the early Middle Ages, mainly thanks to silver mining. Kutná Hora is rightly considered the jewel of the country, its wealth was at the very cradle of the boom of the Czech kingdom. It boasts a variety of architectural styles and unique buildings from different historical periods. Its long history literally breathes on us through every street, house, and church. It is no surprise that Kutná Hora is registered on the UNESCO World Cultural Heritage List. Recent years have also seen a return to the tradition of wine growing, which was once an integral part of the town's colour.

Kutná Hora is located near the capital city of Prague in an easterly direction. It is easily accesible by car (50 km), by train (about 50 minutes from Prague's main railway station), or by bus. When travelling from the east, it is close enough to the D1 highway on the way from Brno (160 km, about 1.5 hours drive). About 21 000 people live in Kutná Hora.

The starting point for most participants will probably be Prague. Prague is located in the heart of Europe. It is an international transport hub, reachable by road, rail, and air. The Václav Havel Airport Prague (PRG/LKPR) offers direct flights to more than 150 destinations around the world, mostly in Europe, but also in the USA, Asia, and Africa.

Prague itself, another UNESCO World Cultural Heritage Site, is certainly worth a visit on the way to or from the conference. After the conference, it is also possible to visit the Astronomical Institute in Ondřejov which is located about 30 km from Prague, near the road between Kutná Hora and Prague.

4 Excursion

For those who will decide to attend IMC 2024 in Kutná Hora, a picturesque place full of history, a guided tour of the town's most important sights will be offered on Saturday afternoon. Professional guides will show you the town and help you uncover its medieval secrets.

Participants will visit St. Barbara's Cathedral, walk through the historic centre of the town, and end the tour at the 'Medieval Central Bank', where they will learn how silver coins were minted in the Middle Ages. The tour last approximately 2.5 hours.

Figure 5 – St. James Church is one of the town's landmarks. Photo credit: Hotel Mědínek.

5 VIP activity

A guided tour will be arranged for those who would like to learn more about silver mining and processing. The 'Way of Silver' tour lasts 1.5 hours and will not be included in the conference fee.

The tour introduces the whole process of medieval mining, the processing of raw silver, and the technology of coinage. It includes a replica of a mining operation with technical equipment, the original large horse-powered mining machine, an authentic medieval mine, and a 'mining settlement'. This offers replicas of log buildings and shelters (known as miners' caverns), ore washing troughs, a replica of a hearth furnace, and a silver ore crushing plant. Equipped with a helmet with a torch and a miner's coat with a hood, you will walk through about 250 metres long part of the original medieval mine.

6 The organizers

The local organising committee is comprised of David Čapek, Tomáš Henych, Pavel Koten (chairman), Lukáš Shrbený, Vlastimil Vojáček, and Hana Zichová. They are all members of the Meteor Physics Group, Department of Interplanetary Matter, Astronomical Institute of the CAS in Ondřejov, a well-known group in the field of meteor science. The Ondřejov Observatory is the centre of the European Fireball Network, the longest-running project for monitoring the bright meteors in the world. Its origins go back to the middle of the 20th century, when Zdeněk Ceplecha, a famous meteor scientist, laid the foundations of this network. The recovery of the Příbram meteorites in 1959 represents the first instrumentally documented meteorite fall in history.

7 Conclusion

Despite the long tradition of meteor research in the Czech Republic, the IMC has never been held in our country. As the members of the Meteor Group have participated in many IMCs in the past, we would now like to invite the international meteor community to our country and give them the opportunity to meet at this traditional meeting. That's why we would like to welcome you in Kutná Hora, a beautiful historical mining town.

More information about the conference will be available soon on its website (`https://imc2024.imo.net/`).

Ongoing meteor work

Meteor Spectroscopy: Visual Lookup for Elemental Abundances

Joe Zender[1], *Detlef V. Koschny*[2], *Regina Rudawska*[3], *and Stefan Loehle*[4]

We observe an increased effort of amateurs and professionals to acquire meteor spectra in the visual wavelength in the past years. To allow a first identification of the chemical elements of the observed spectra, the paper provides a list of plots that allow this identification. As the origin of the elements can be meteoric or atmospheric which are exposed to different temperature regimes, the plots are provided for the 'warm' component for meteoric elements and the 'hot' component for atmospheric elements.

Received 2023 December 8

This work has been presented at the International Meteor Conference 2023.

1 Introduction

Meteor spectroscopy allows the identification and quantitative analysis of dust grains passing through the Earth atmosphere. Several groups around the globe acquire meteor spectra either campaign-driven (Koschny et al., 2012; Vaubaillon et al., 2015), or on permanent basis (Koschny et al., 2013; Tóth et al., 2015), typically based on the technology of video imaging and spectral gratings. Source data are images either acquired as individual exposures (long exposures) or as individual frames (short exposures) obtained from a video stream. The images contain the first order spectrum of the meteor. After the radiometric and geometric calibration of the images the spectral information is extracted as an intensity line plot. The quantitative analysis of these intensity plots requires the optimization of several parameters:

- the wavelength of the intensity plot,
- the existence of a chemical element to contribute to the line plot,
- the number density of atoms or molecules of each identified element contributing to the emission,
- the contribution of the absorption by the vaporized ablation cloud,
- the assumed temperature or temperatures of the ablation,
- the line broadening of the optical system.

All these parameters have been widely discussed in (Jenniskens, 2007; Ceplecha, 1971; Borovicka, 1994; Vojáček et al., 2015; Zender et al., 2023).

Meteoroids ablate in the Earth atmosphere at temperatures in the range of several thousands Kelvin. Caused by the high entry velocity, a shock wave is created in front of the meteor with a temperature of several ten thousands of Kelvin. The size and form of the shock wave and the relating temperatures are dependant on the entry velocity and angle of the meteoroid in respect of the atmosphere. A model for artificial particles was developed by Vovk et al. (2023) and the authors provide a visual representation here as Figure 1 (Figure 4 in Vovk et al. (2023)).

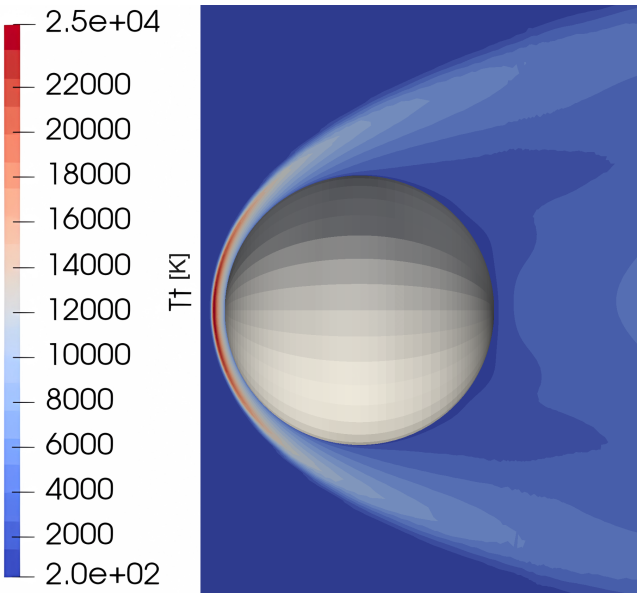

Figure 1 – A model for temperature regimes of the meteor and the related shock wave as provided in Vovk et al. (2023).

For a first identification of chemical elements, the authors typically use the tables provided in Jenniskens (2007) and Borovicka (1994). The intensities for the elements is given for 4000 K for the 'warm' component and 10000 K for the 'hot' component. From Figure 1 it must be understood that the temperatures are not fixed temperatures but instead the 'warm' and 'hot' components represents ranges of temperatures, as e.g. discussed in Jenniskens et al. (2004).

[1]European Space Research and Technology Center (ESTEC), 2200 AG Noordwijk, The Netherlands.
Email: Joe.Zender@esa.int
[2]TU Munich, Germany
[3]THEA Group, ESA/ESTEC, The Netherlands
[4]High Enthalpy Flow Diagnostics Group (HEFDiG), Institute of Space Systems, University of Stuttgart, Pfaffenwaldring 29, 70569 Stuttgart, Germany

IMO bibcode WGN-516-zender-spectroscopy
NASA-ADS bibcode 2023JIMO...51..146Z

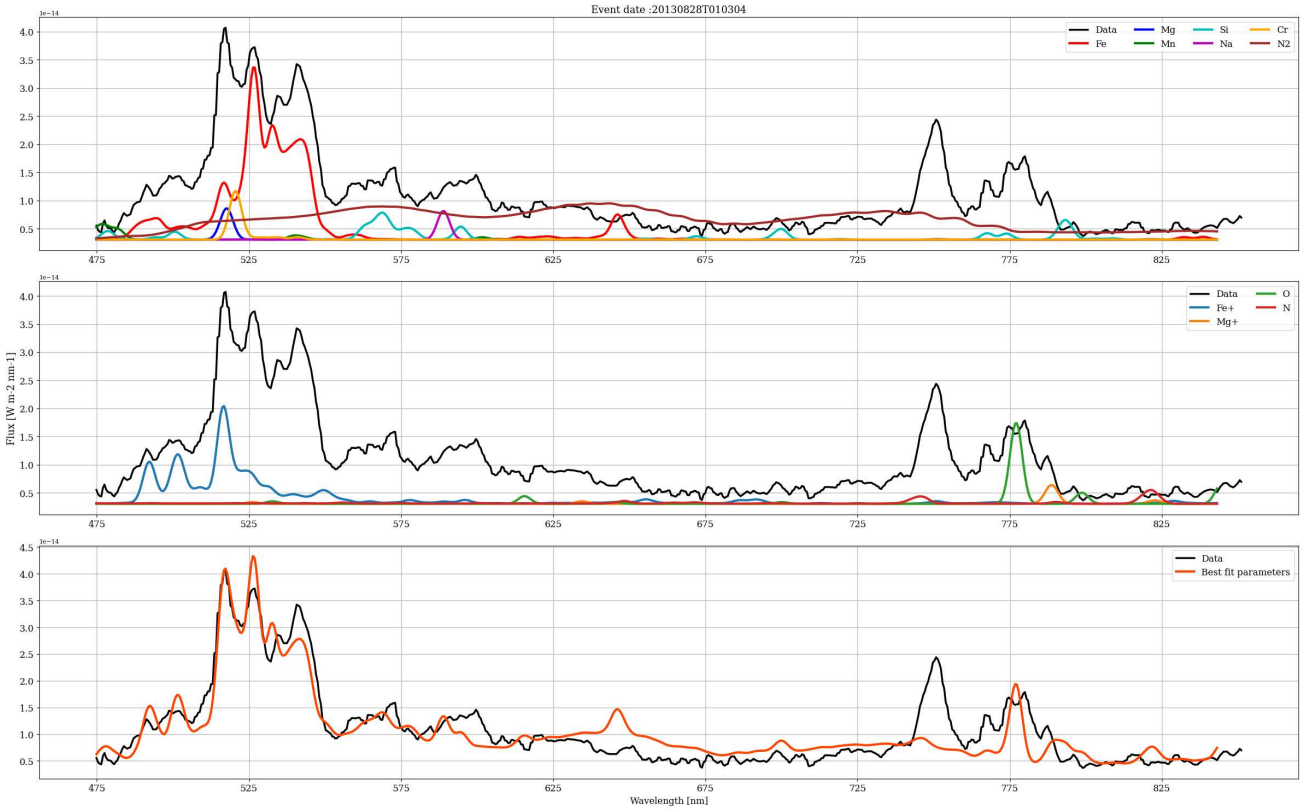

Figure 2 – Sporadic meteor observed on 20130828T010304, the three plots represent simulations at 4000 Kelvin, 10000 Kelvin, and the superposition of the two temperature simulations (from top to bottom).

2 Spectral Response Profiles for Meteoric and Atmospheric Elements

The individual line profiles of the elements shown in the following figures were produced by ESA's PlasmA RAdiation DatabasE (PARADE) tool, originally used to simulate variation of probe entries into planetary atmosphere's (Smith, 2006). PARADE calculates the energy state transitions in atoms and molecules and provides the emission coefficient ϵ in radiance, with the unit $W/m^2/sr$ (Loehle et al., 2021; Zender et al., 2023). The figures presented contain four subplots, each for one element. For each element the line intensities obtained at 4000 K are provided in $W/m^2/sr$. For the main peak(s) in the spectrum, the intensity evolution at the peak wavelength(s) is computed over a temperature ranging from 2500 K to 5000 K for the 'warm' component and from 9000 K to 13000 K for the 'hot' components. The temperature range is provided in the top-level x-axis and the intensity at the right-side y-axis. The plots in each section are listed in the order of maximum intensity, thus the faintest responses are listed first and the last subplot contains the highest peak intensity value. Each subplot will allow for the respective element

- the identification of the main intensity or – in case the element ablates with multiple intensity peaks – the main two or three intensities,
- the intensity evolution of the main peak(s) over a given temperature range.

2.1 Discussion of one Example

We provide the discussion of one sporadic meteor that was observed at Teneriffe on 2010828T010304. Figure 2 shows three subplots each showing as a black-colored profile the calibrated spectrum of the meteor. The top-level plot contains the response of a few elements simulated at 4000 Kelvin, the middle-plot a few elements simulated at 10000 Kelvin, and the bottom-plot the superposition of the both temperature components. The individual elements are color-coded as given in the legend of the image in the top-right corner.

Here follows a discussion with the goal to interpret the given spectrum. The reader shall take note that other interpretations than the one given might be possible.

- The spectrum in the range from 500 to 775 nm is characterized by an uplift. Comparing with the atmospheric responses as given in Figure 11, the uplift might be due to the warm component of N2.
- The interpretation of the two spectral peaks below 500 nm is difficult, as several elements have spectral maxima in this region. Assuming that the maxima at 510 nm is a Fe^+ line (see Figure 8), then the Fe^+ can explain the three peaks below 510 nm, as shown in the middle-plot.
- If there is an indication of Fe^+, surely there should be a response of Fe in the warm component. The spectral response of the Fe-15 triplet as shown in Figure 6 fits well the peaks from 526 to 550 nm.

- The peak at 510 nm is build up from three elements (Mg, Cr, Fe) at the warm component, and the Fe-ions.
- The peak at 746 nm could be a response from atmospheric nitrogren (see Figure 9). N has however another, even stronger peak at 821 nm. This peak is not observed in our spectrum which might be explained by the lack of spectral sensitivity above 800 nm. As the used algorithm currently tries to fit all maxima, the maxima at 746 nm is not identified.
- The atmospheric oxygen line at 777 nm is often a typical peak in the meteor spectra. In the case of our example, the oxygen can explain only a part of the spectral increase seen between 760 and 790 nm.
- The identification of the other elements shown in the legend of Figure 2 is questionable, and not further discussed.

2.2 Atomic Responses

The reader shall take note that the iron atom has several intensity maxima and strong emissions are in the visual (above 400 nm) and the Ultraviolet (UV, below 400 nm). As the Earth atmosphere absorbs most of the UV radiation at an altitude above 90 km and partially below, the UV part of the iron emission can only be observed for the meteor ablation phase below this altitude (Vicinanza et al., 2021). As the spectral response of our camera system was derived from star calibration (Vicinanza et al., 2021; Zender et al., 2023), the wavelength below 400 nm is effected by the atmospheric absorption resulting in a potential over-amplification this part of the spectrum. For this reason we provide the iron responses above 400 nm as FeI-15 (the iron 15 multiplet) and below 400 nm as Fe. Please see the spectral responses in Figure 3 (He, F, Ar, Ni), Figure 4 (Si, K, Ti, Mn), Figure 5 (V, C, Cr, Mg), and Figure 6 (Fe, Ca, Na, FeI-15).

2.3 Responses of Meteoric Molecules at 4000 K

Please see the spectral responses in Figure 7 (CO, CH, CN, NH).

2.4 Responses of Ionized Elements

The intensity plots of ionized sodium, carbon, iron, and argon are given in Figure 8 for the hot environment (10000 K).

2.5 Responses of Atmospheric Elements

At an atmospheric entry altitude between 70 km and 90 km there is a significant degree of thermochemical non-equilibrium. Following Smith (2006), the density at 70 km is 7.9×10^{-5} kg/m^3 and the temperature 218 K. Peak post shock translational temperatures can approach 30000 K, while the shock layer equilibrium temperature is approximately 16000 K. At these conditions the flow is significantly ionised, and we consider 8 air species, those being N_2, N, O_2, O, NO, N_2^+, N^+, and O^+. As the air species can show excitations at any temperatures, we provide the plots for the 'warm' case (Figure 9 and Figure 10) first, followed by the plots for the 'hot' case (Figure 11 and Figure 12).

2.6 Conclusion

We have provided a list of plots showing the emission profiles of several chemical elements that might be contained in meteoroids and or that are present in the Earth atmosphere. These plots allow a first identification of the elements contained in a meteor spectrum.

References

Borovicka J. (1994). "Two components in meteor spectra". *Planetary and Space Science*, **42:2**, 145–150.

Ceplecha Z. (1971). "Spectral data on terminal flare and wake of double-station meteor No. 38421 (Ondřejov, April 21, 1963)". *Bulletin of the Astronomical Institutes of Czechoslovakia*, **22**, 219.

Jenniskens P. (2007). "Quantitative meteor spectroscopy: Elemental abundances". *Advances in Space Research*, **39:4**, 491–512.

Jenniskens P., Laux C. O., Wilson M. A., and Schaller E. L. (2004). "The Mass and Speed Dependence of Meteor Air Plasma Temperatures". *Astrobiology*, **4:1**, 81–94.

Koschny D., Bettonvil F., Licandro J., van der Luijt C., Mc Auliffe J., Smit H., Svedhem H., de Wit F., Witasse O., and Zender J. (2013). "A double-station meteor camera set-up in the Canary Islands - CILBO". *Geoscientific Instrumentation, Methods and Data Systems*, **2:2**, 339–348.

Koschny D. V., McAuliffe J., Bettonvil F. C. M., Gritsevich M., van der Luijt C., Ocaña F., Smit H., Svedhem H., and Zender J. J. (2012). "What happened at ESA's Meteor Research Group in 2010/11?". In *Proceedings of the International Meteor Conference, 30th IMC, Sibiu, Romania, 2011.* pages 57–60.

Loehle S., Eberhart M., Zander F., Meindl A., Rudawska R., Koschny D., Zender J., Dantowitz R., and Jenniskens P. (2021). "Extension of the plasma radiation database PARADE for the analysis of meteor spectra". *Meteoritics & Planetary Science*, **56:2**, 352–361.

Smith A. J. (2006). "Plasma radiation database parade v2.2, Technical Report TR 28/96 Issue 3.". Technical report, Emsworth, UK: Fluid Gravity Engineering Ltd.

Tóth J., Kornoš L., Zigo P., Gajdoš Š., Kalmančok D., Világi J., Šimon J., Vereš P., Šilha J., Buček M., Galád A., Rusňák P., Hrábek P., Ďuriš F., and Rudawska R. (2015). "All-sky Meteor Orbit System AMOS and preliminary analysis of three unusual meteor showers". *Planetary and Space Science*, **118**, 102–106.

Vaubaillon J., Koten P., Margonis A., Toth J., Rudawska R., Gritsevich M., Zender J., McAuliffe J., Pautet P.-D., Jenniskens P., Koschny D., Colas F., Bouley S., Maquet L., Leroy A., Lecacheux J., Borovicka J., Watanabe J., and Oberst J. (2015). "The 2011 Draconids: The First European Airborne Meteor Observation Campaign". *Earth Moon and Planets*, **114:3-4**, 137–157.

Vicinanza S., Koschny D., Rudawska R., Stam D., van der Wal W., and Zender J. (2021). "Spectral Calibration of Meteors: An Elevation-Dependent Atmospheric Correction". *WGN, Journal of the International Meteor Organization*, **49:6**, 201–210.

Vojáček V., Borovička J., Koten P., Spurný P., and Štork R. (2015). "Catalogue of representative meteor spectra". *Astronomy & Astrophysics*, **580**, A67.

Vovk M., Koschny D., Frühauf M., Gscheidle C., Hugentobler U., Heumann V., Lips T., Fritsche B., Maigler M., Pessina V., Šilha J., Tóth J., Pazderová V., and Matlovič P. (2023). "Meteoroid ablation simulations with ESA's SCARAB software". *Planetary and Space Science*, **238**, 105785.

Zender J., Koschny D., Rudawska R., Vicinanza S., Loehle S., Eberhart M., Meindl A., Smit H., Marraffa L., Landman R., and Stam D. (2023). "Spectral observations at the Canary Island Long-Baseline Observatory (CILBO): calibration and datasets". *Geoscientific Instrumentation, Methods and Data Systems*, **12:1**, 91–109.

Handling Editor: Javor Kac
This paper has been typeset from a LaTeX file prepared by the authors.

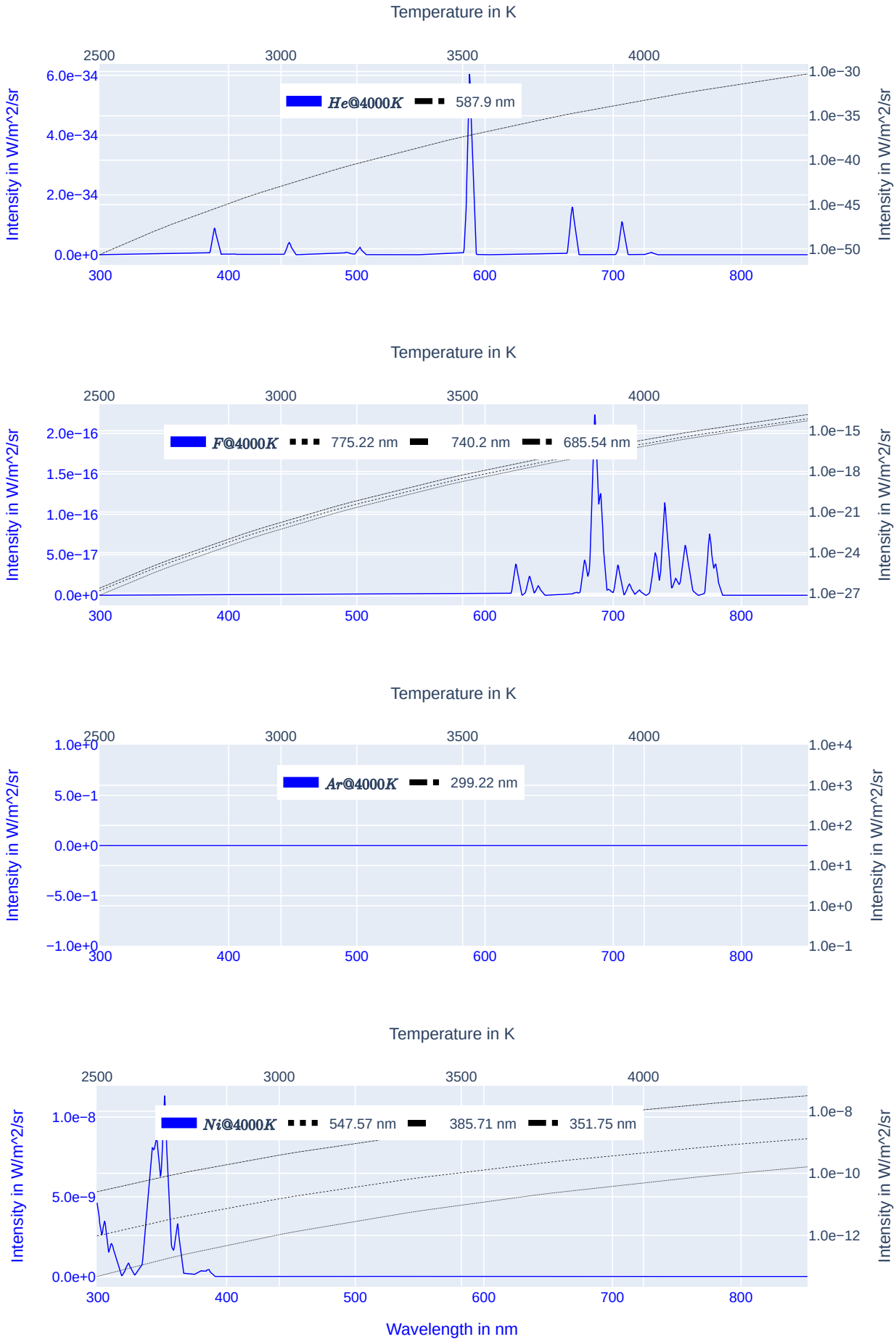

Figure 3 – He, F, Ar, and Ni spectral response profiles at 4000 K.

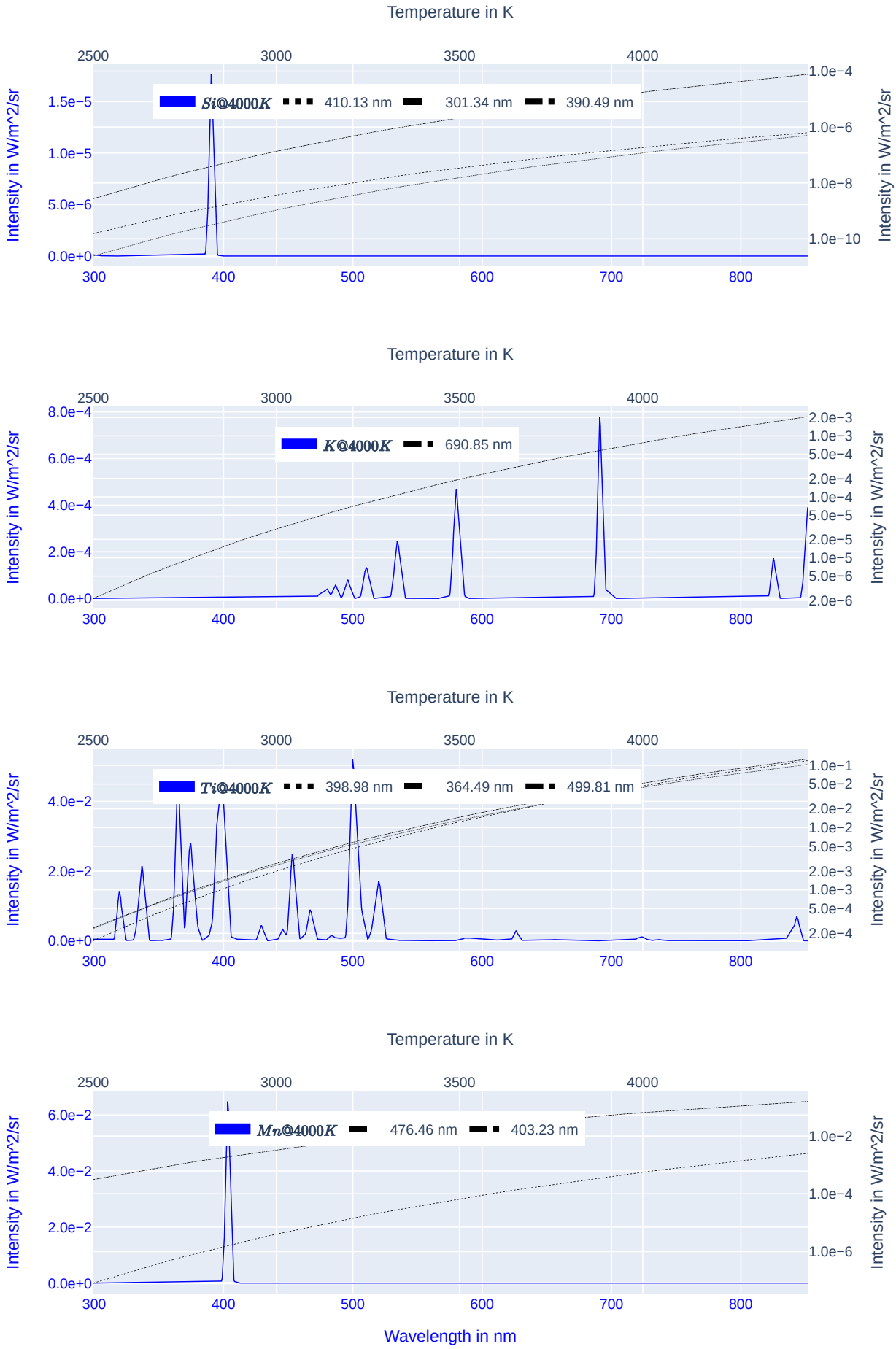

Figure 4 – Si, K, Ti, and Mn spectral response profiles at 4000 K.

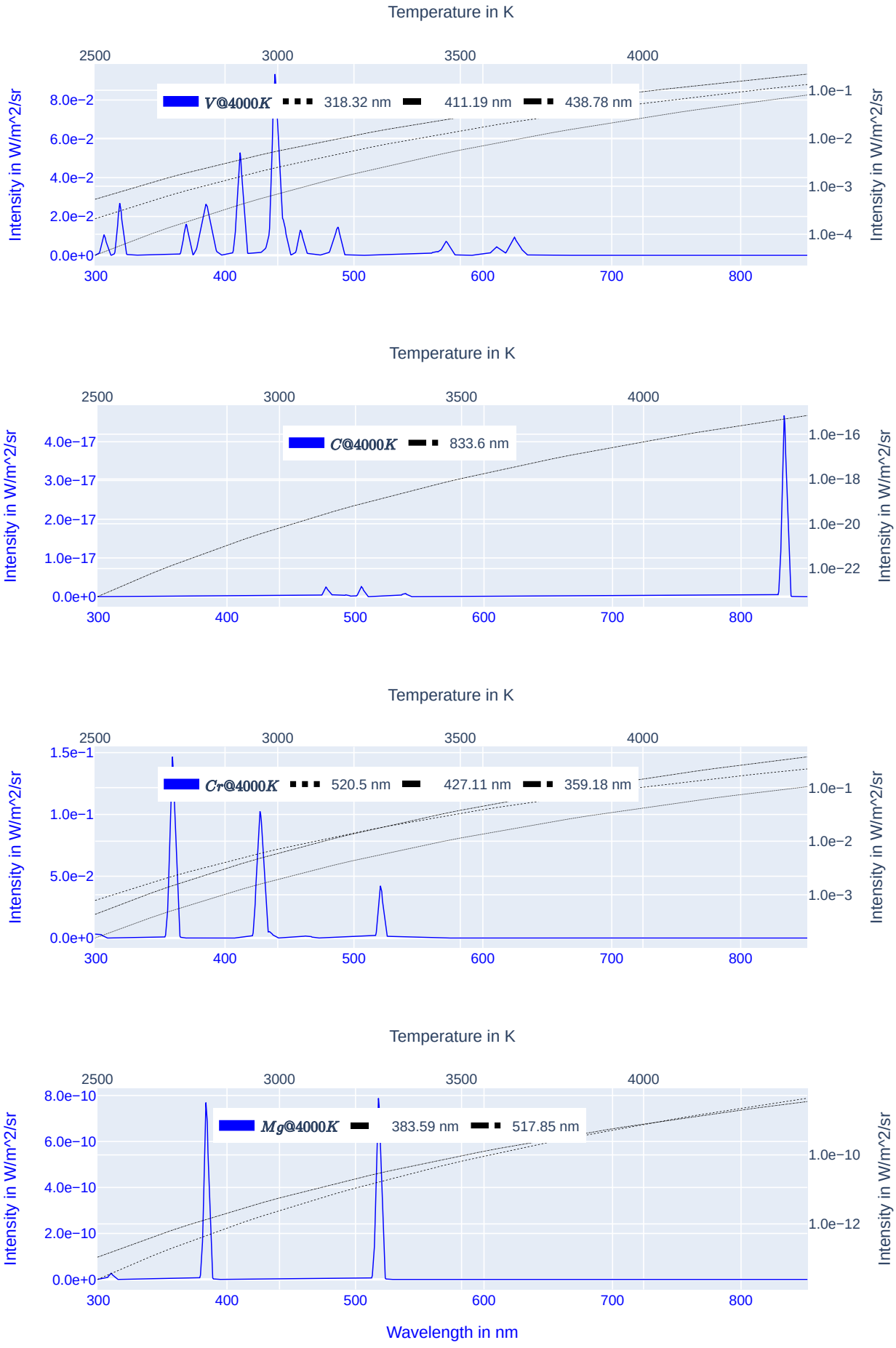

Figure 5 – V, C, Cr, and Mg spectral response profiles at 4000 K.

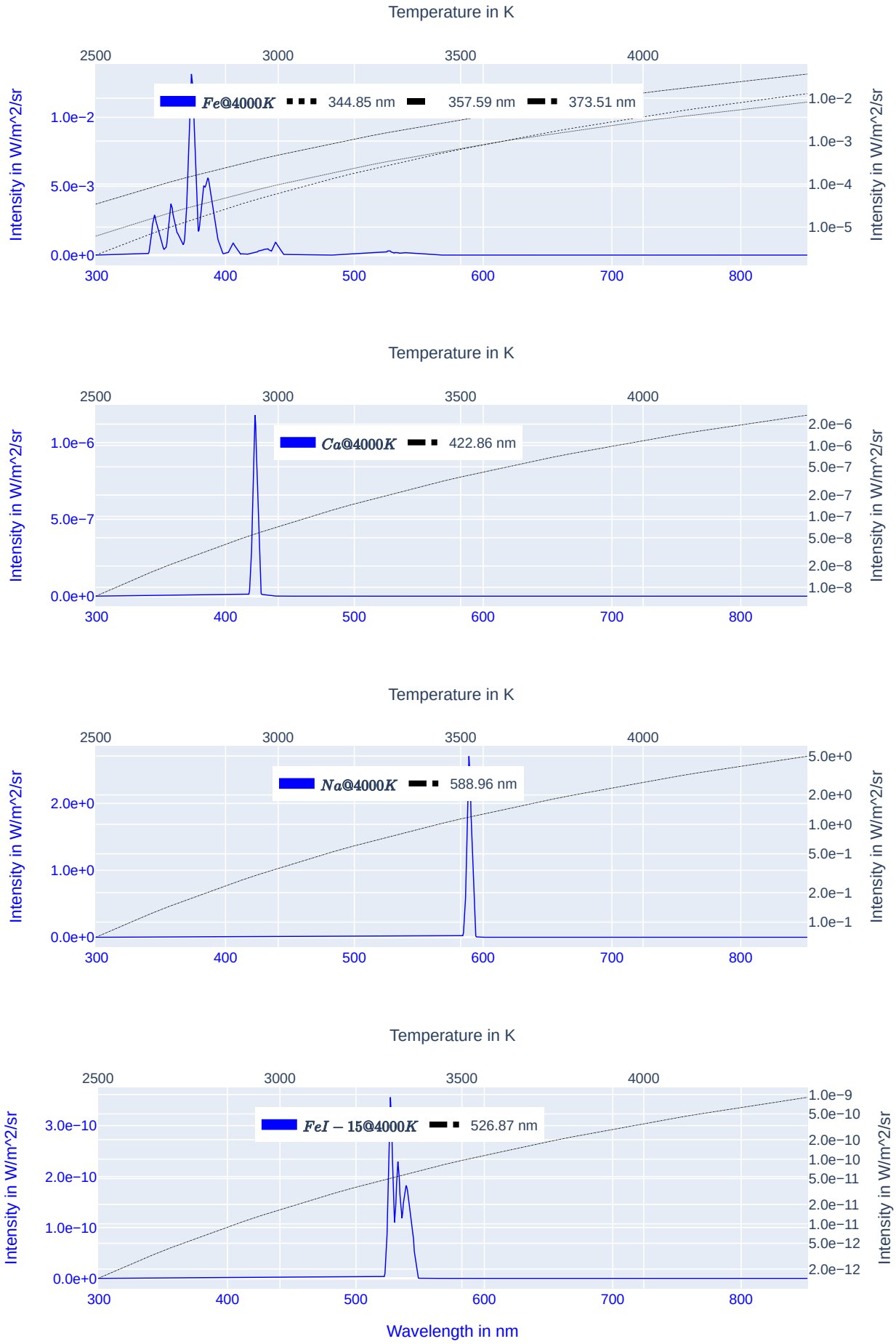

Figure 6 – Fe, Ca, Na, and FeI-15 spectral response profiles at 4000 K.

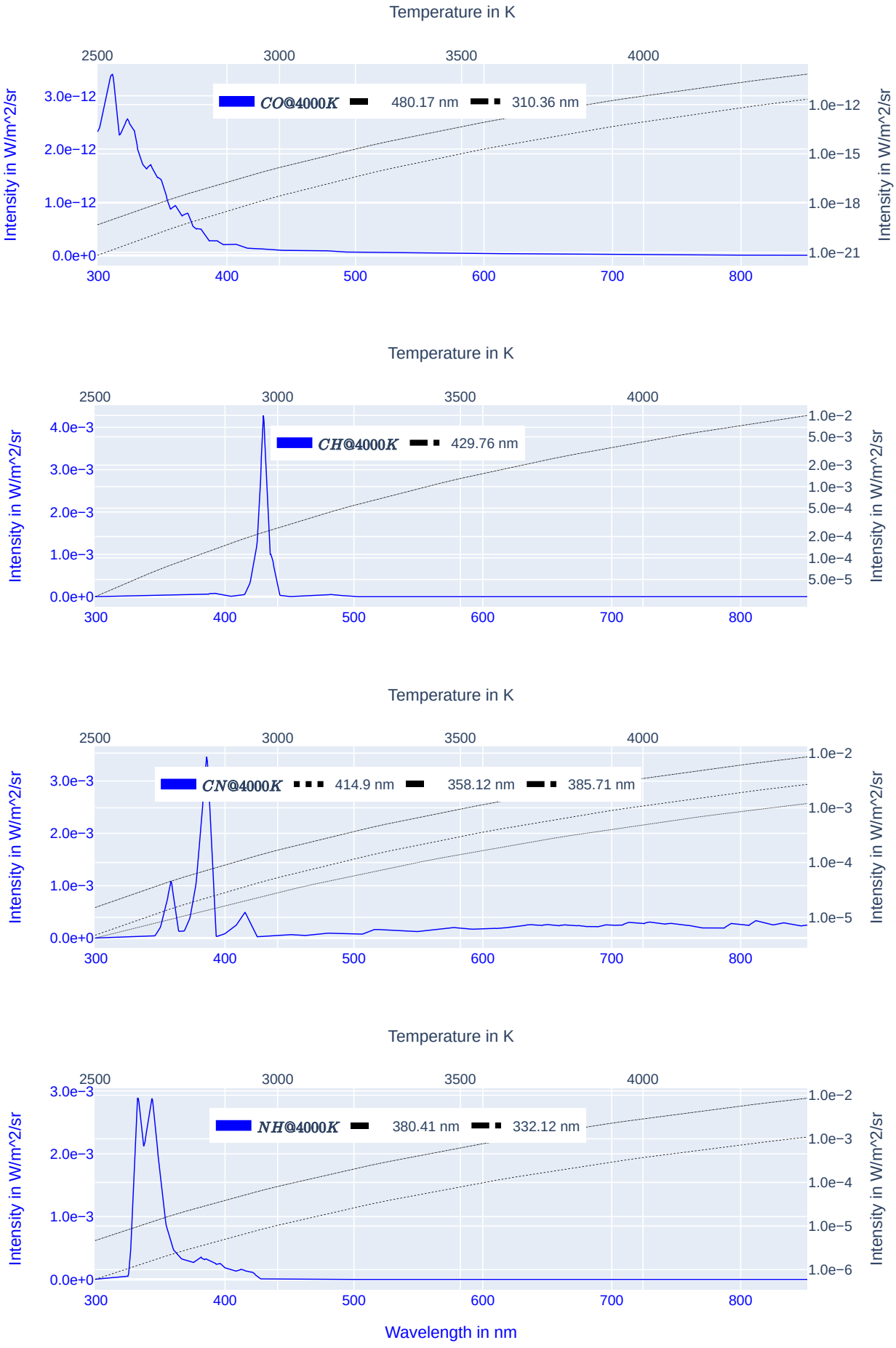

Figure 7 – CO, CH, CN, and NH spectral response profiles at 4000 K.

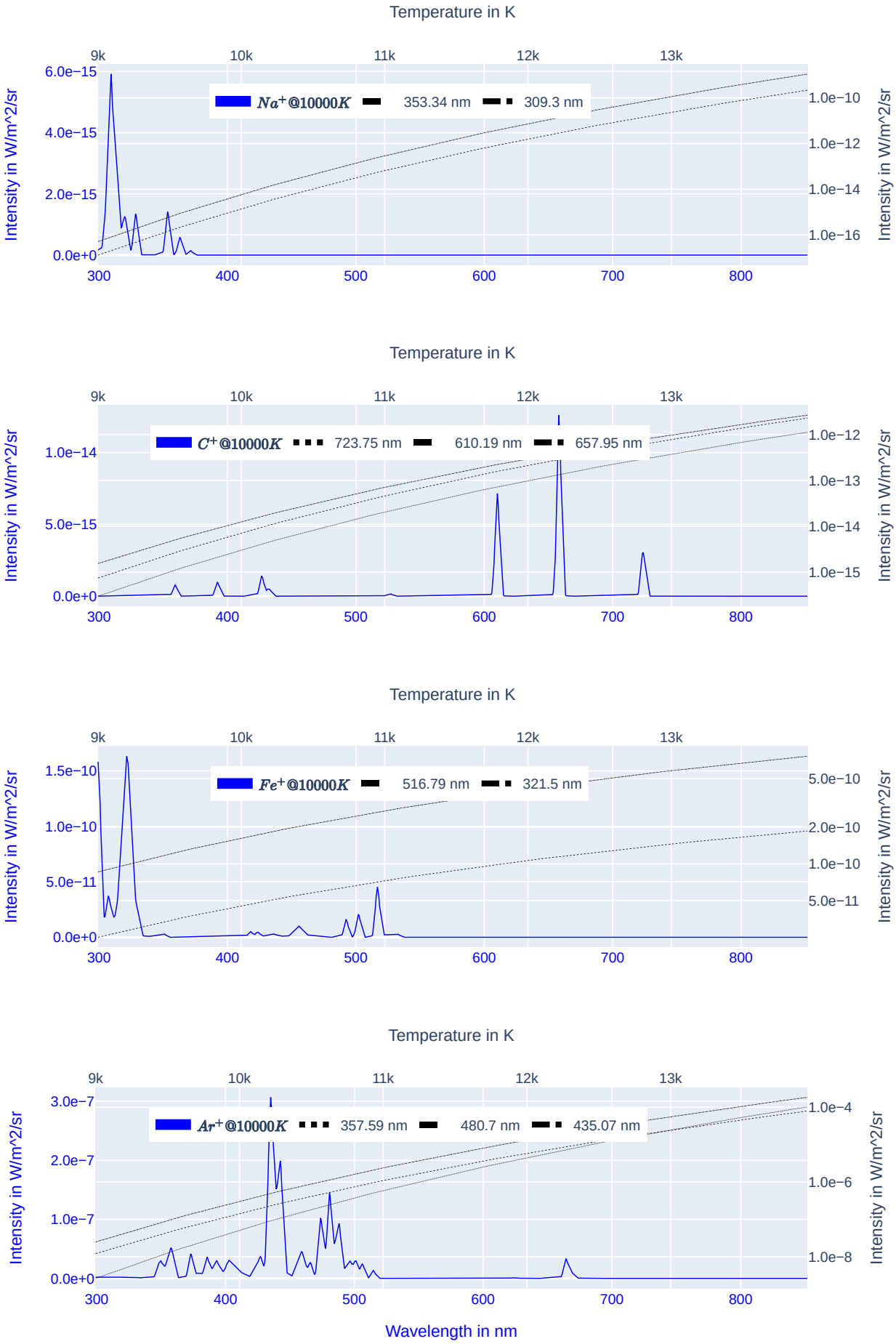

Figure 8 – Na^+, C^+, Fe^+ and Ar^+ spectral response profiles at 10000 K.

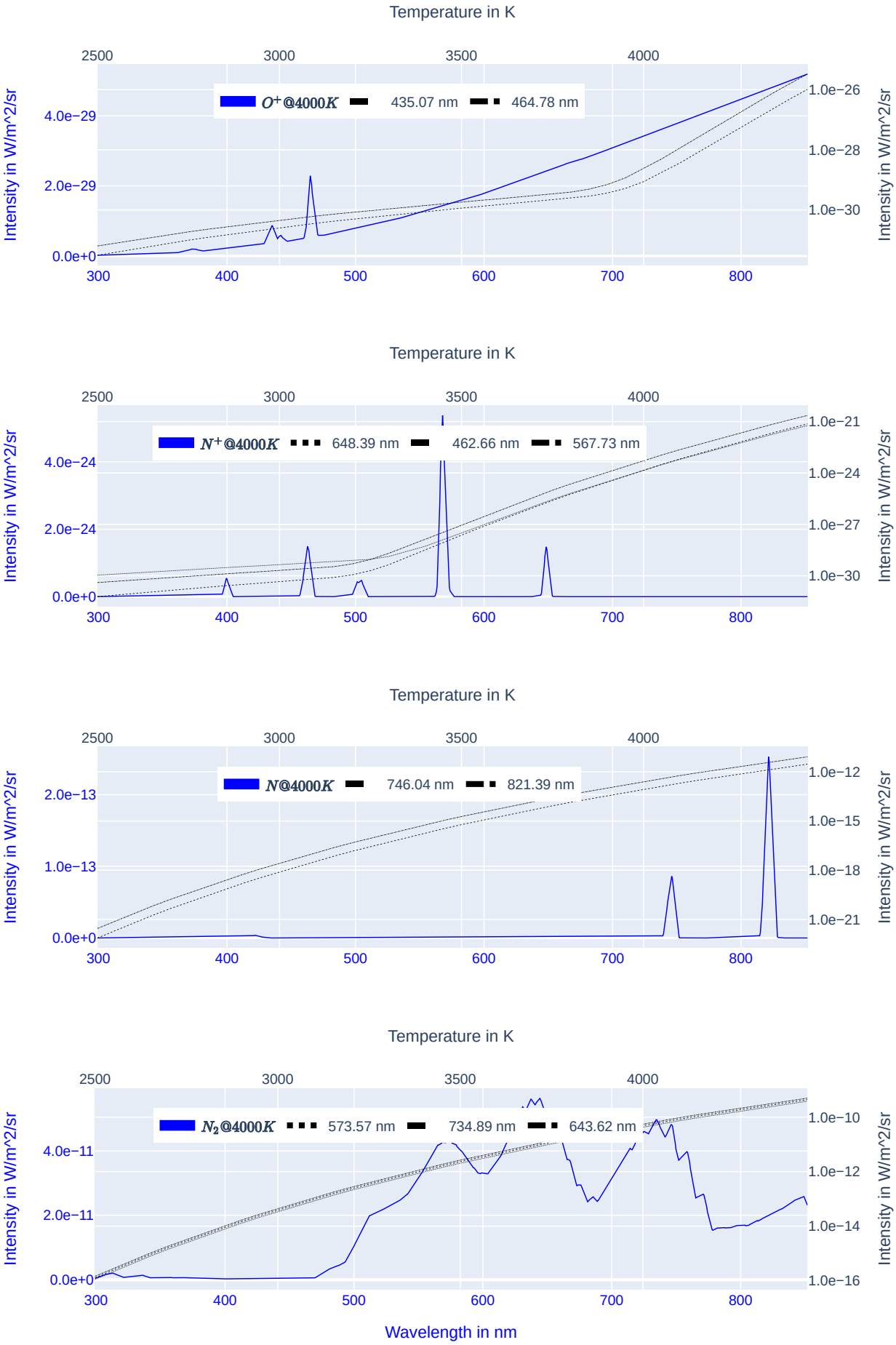

Figure 9 – O^+, N^+, N, and N_2 spectral response profiles at 4000 K.

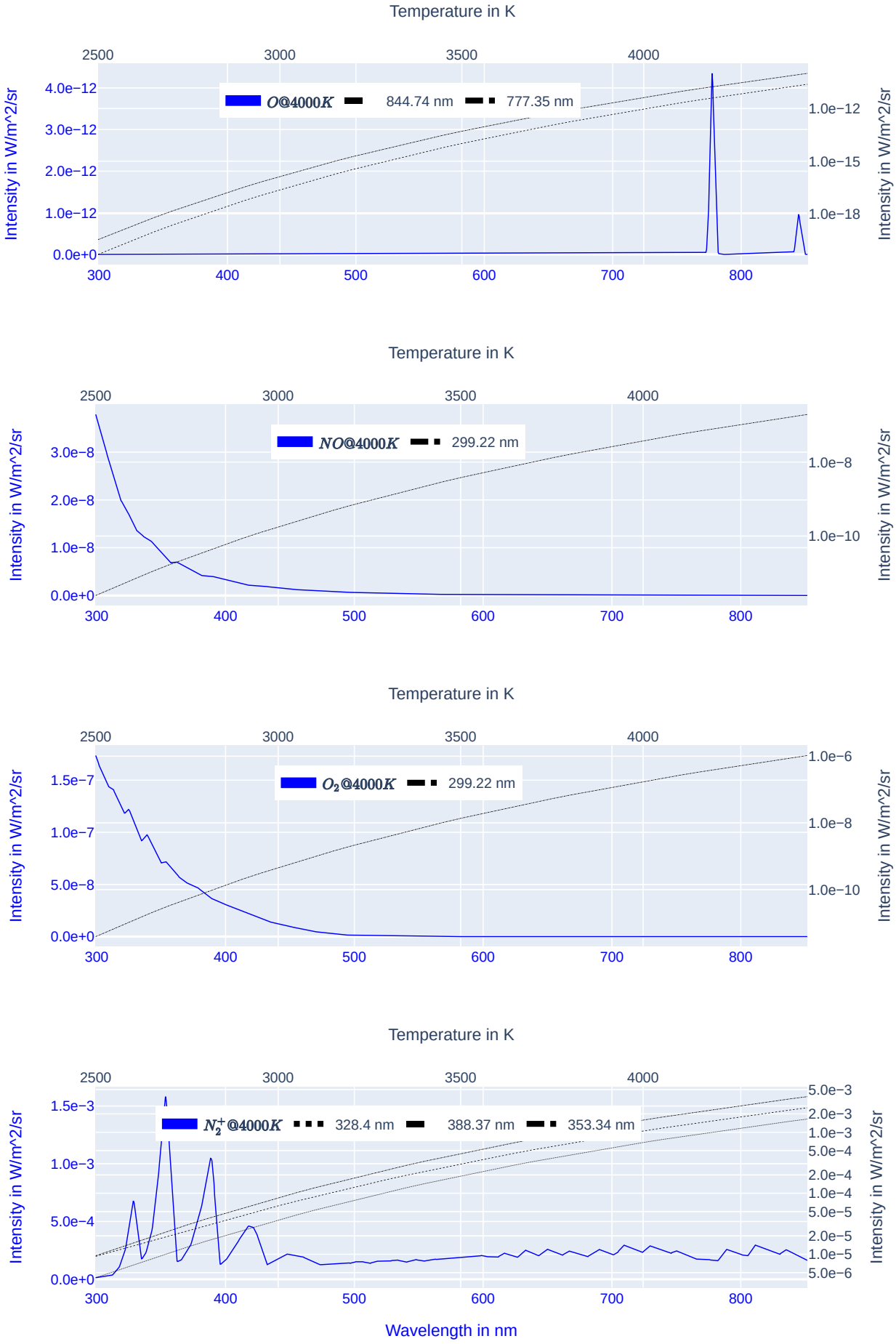

Figure 10 – O, NO, O_2, and N_2^+ spectral response profiles at 4000 K.

Figure 11 – O^+, N^+, N, and N_2 spectral response profiles at 10000 K.

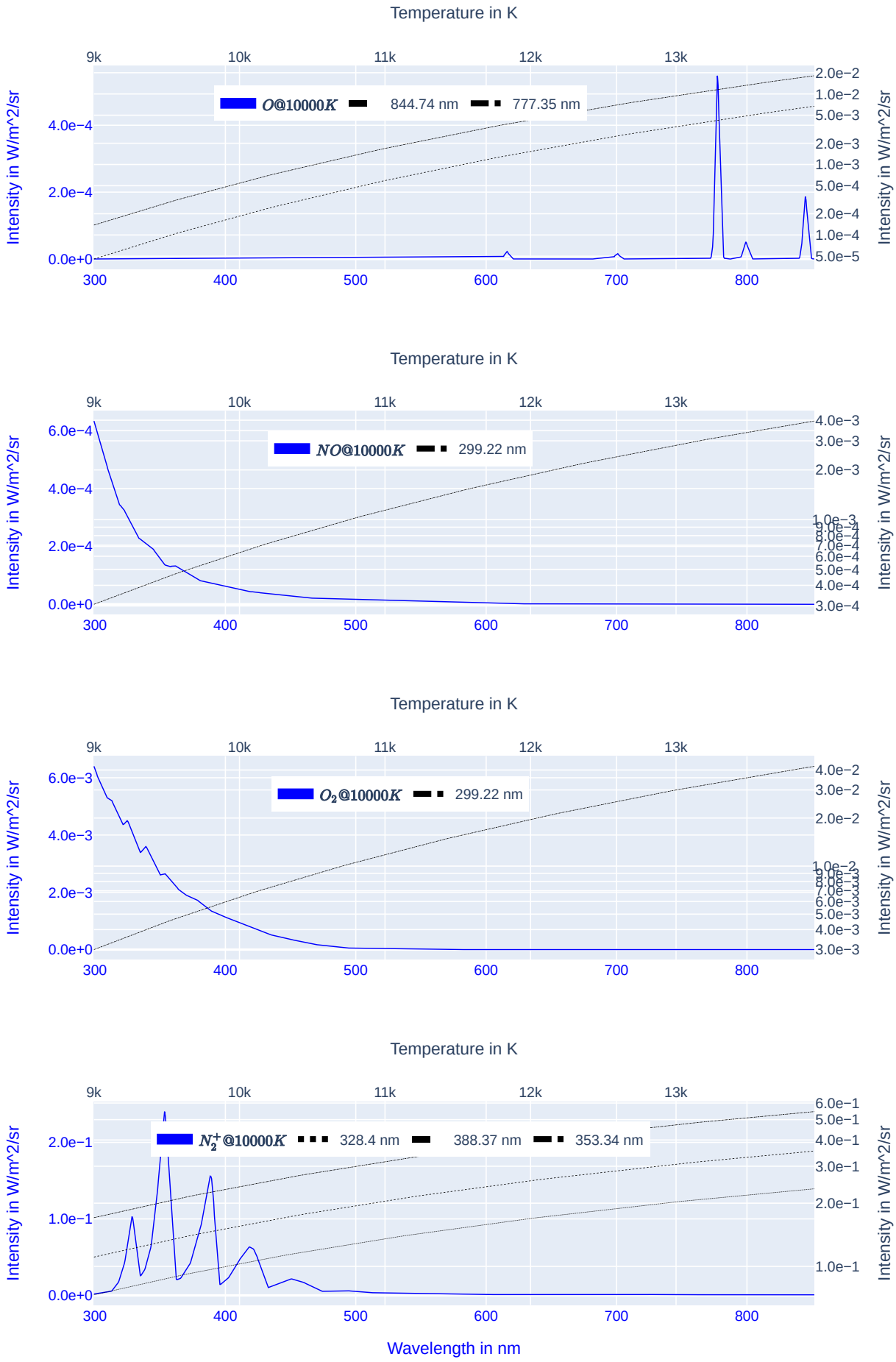

Figure 12 – O, NO, O_2, and N_2^+ spectral response profiles at 10000 K.

August delta-Capricornids 2022 observations by CAMS

Tim W. Beck[1]*, Peter Jenniskens*[2]*, and the CAMS team*

We report on the 2022 August 16–17 CAMS detection of a predicted encounter with debris ejected by parent comet 45P/Honda-Mrkos-Pajdušáková in 1980. This was the first time that a meteor shower associated with this comet was observed. The observations demonstrate that cm-sized dust is associated with this comet. The shower was already in the IAU Working List of Meteor Showers as IAU number 199, the August delta-Capricornids, based on uncertain prior detections of meteors in similar orbits to that of the comet.

Received 2023 November 12

This work has been presented at the International Meteor Conference 2022.

1 Introduction

Jupiter-family comet 45P/Honda-Mrkos-Pajdušáková (Figure 1) moves in a low-inclination ($i = 4.2°$) orbit with perihelion distance well inside Earth's orbit ($q = 0.53$ AU). The orbit passes relatively close to the orbits of Earth and Venus and meteor shower activity has been predicted for both planets (e.g., Jenniskens, 2006; Vaubaillon & Christou, 2006).

The comet was discovered in 1948 and was observed during the returns in 1954, 1964, 1969, 1974, 1980, 1990, 1995, 2001, 2006, 2011 and 2016 (e.g., Wlodarczyk, 2022). Radar observations during the 2016 return shows it has a 1.3-km large nucleus that rotates with a spin rate of 7.6 h (Springmann et al., 2017; Springmann et al., 2022).During each rotation, it has repeated CN and C_2 emissions in the form of a jet with gas projected away from the nucleus with an outflow velocity of 0.5 km/s (Springmann et al., 2022). It emits large (> 2 cm) grains (Springmann et al., 2017), which would cause visible meteors when impacting Earth. The comet was observed by the SWAN camera on the SOHO satellite in 2001, 2011 and 2017, during which time the comet activity has remained similar, with no long-term fading or abrupt decreases (Combi et al., 2020).

The August delta-Capricornids (#199, ADC) meteor shower was first detected by Terentjeva (1989), her shower 43, from a D-criterion search among fireball streams. She found meteors in similar orbits radiating from R.A. = 324.°7, Decl. = −13.°8 (B1950) and $V_g = 22.0$ km/s during August 13–31, and gave the name "δ-Capricornids". Porubcan & Gavajdova (1994) in a D-criterion search among 1 000 photographed orbits of meteors brighter than −3 also found a stream with orbital elements similar to 45P. Given the large number of anthelion meteors in similar orbits, a link with comet 45P was proposed, but remained uncertain (Jenniskens, 2023).

Figure 1 – Comet 45P in a photo by Michael Jäger (with permission) on 2011 29 September.

The dust trail model by S. Shanov and S. Dubrovski in Jenniskens (2006) put the 1969 dust of 45P in Earth's path on 2015 August 14, at $\lambda_\odot = 140.°990$ radiating from R.A. = 325.°8, Decl. = −10.°7 with $V_g = 25.63$ km/s, but that event was not observed.

Maslov (2020) named the shower "χ-Capricornids" and predicted encounters with dust trails of 45P in 2010, 2014 and 2019, but with difficult to observe properties and none were detected. Conditions were better for 2022, when he predicted an encounter with the 1980-dust ejected by 45P on 16 August at 23^h40^m UT (solar longitude $\lambda_\odot = 143.°772$), with the dust passing Earth's orbit at 0.00377 AU, and requiring an ejection speed of 9.82 m/s to put the dust far enough ahead of the comet. The predicted radiant was given as R.A. = 326.°8, Decl. = −15.°1. The radiant would be placed well for most network locations throughout the night, with best viewing predicted for Namibia. The 0.72 phase Moon would create some light pollution, with 2-3 hours of dark skies in the early evening hours (Maslov, 2020).

The outburst was first detected on August 15/16, and then again on 16/17, by the CAMS low-light video networks (Jenniskens, 2022a; Jenniskens, 2022b), which suggested two activity periods. Because earlier predictions of dust trail crossings from 45P had not panned out, the source of the outburst was initially unclear. The main outburst was confirmed from SonotaCo data

[1]Mendocino Community College, Ukiah, CA 95482, USA.
Email: tbeck@mendocino.edu
[2]SETI Institute, 339 Bernardo Ave, Mountain View, CA 94043, USA.
Email: pjenniskens@seti.org

IMO bibcode WGN-516-beck-adc
NASA-ADS bibcode 2023JIMO...51..160B

by Sekiguchi (2022), who identified the outburst as having been caused by comet 45P, and from Global Meteor Network data by Roggemans et al. (2022).

Here, we re-visit and expand on the CAMS network observations.

2 The CAMS network

2.1 CAMS California

CAMS was founded in 2010 with the first stations at Fremont Peak Observatory, Lick Observatory, and in Sunnyvale in California. This CAMS California network has since expanded with stations in Northern California, including in Foresthill. In 2021, a 4-camera station in Windsor was expanded to a full 16-camera station. Small 8-camera stations were established in Mendocino County (Ukiah Latitude Observatory) and Lake County (Taylor Observatory) in 2023.

2.2 Global CAMS networks

The CAMS network has since expanded to 14 other locations in the world and there are now some 600 cameras that monitor the night sky in an effort to triangulate the trajectory and speed of meteors and determine the pre-entry orbit in space. In 2019, the network was expanded with 3-station 16 cameras each in Australia, Chile and Namibia. The results of the triangulations are posted for network coordination purposes the next night at the website `http://cams.seti.org/FDL/`, and also presented to the public at `https://meteorshowers.seti.org`.

Figure 2 shows all meteors detected on August 16/17 by CAMS Namibia. The following CAMS networks triangulated meteors from the August delta-Capricornids shower: 82 meteors were triangulated by network #17 CAMS Namibia (coordinated by T. Hanke, station operators E. Fahl and R. van Wyk), 11 by network #16 CAMS Chile (S. Heathcote, E. Jehin, station operator T. Abbott), 9 by #7 LO-CAMS (coordinated by N. Moskovitz), 9 by #3 CAMS BeNeLux (coordinated by C. Johannink and M. Breukers), 7 by #1 CAMS California (station operators J. Albers, T. Beck, E. Egland, B. Grigsby, and J. Wray), 5 by #2 CAMS Florida (coordinated by A. Howell), 5 by #8 CAMS South Africa (T. Cooper, P. Mey), 4 by #14 CAMS Arkansas (coordinated by L. Juneau, with one station operated by S. Austin), 3 by #20 CAMS Texas (coordinated by W. Cooney), and 1 by #7 the UAE Astronomical Camera Network (coordinated by M. Odeh).

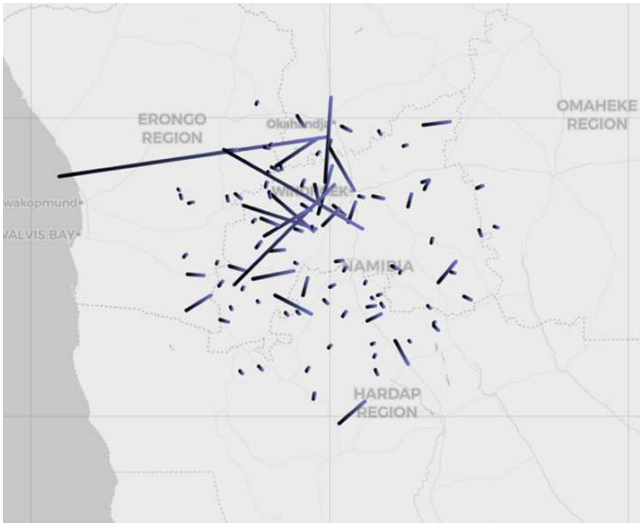

Figure 2 – Detected meteors over Namibia in the night of 2022 August 16/17.

3 Results

137 meteor orbits from this shower were triangulated. They form a well defined cluster in the anthelion source (Figure 3, which includes SonotaCo and Global Meteor Network data). A representative sample of orbital elements is given in Tables 1 and 2.

The magnitude size distributions (From −4 magnitude up in steps of 1 magnitude): 2, 2, 2, 9, 21, 36, 40, 24, 1. Based on the detection probability curve derived from the alpha Capricornids, with similar entry speed and location in the anthelion source, the magnitude size distribution index was $\chi = 2.20 \pm 0.15$ (Jenniskens, 2023).

Based on the deceleration parameters, the meteoroids with early beginning heights ($N = 124$) had an average density of 0.28 g/cm^3 (Jenniskens, 2023). A zero magnitude meteor would be 0.25 g, or 1.2 cm in diameter. Hence, most meteors detected were smaller

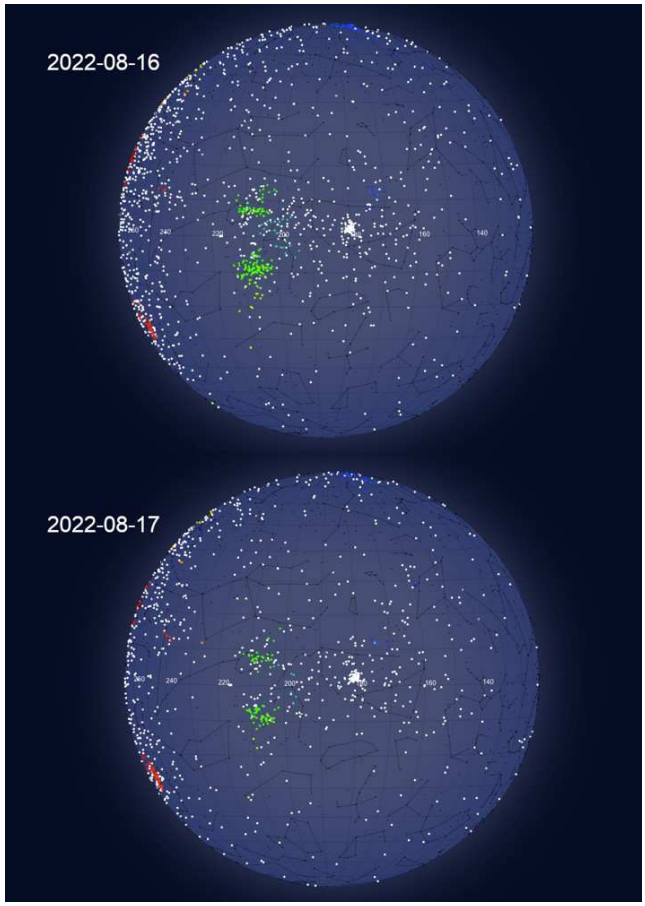

Figure 3 – Combined global video data of ADC (white blob at center) on nights of August 15/16 and 16/17.

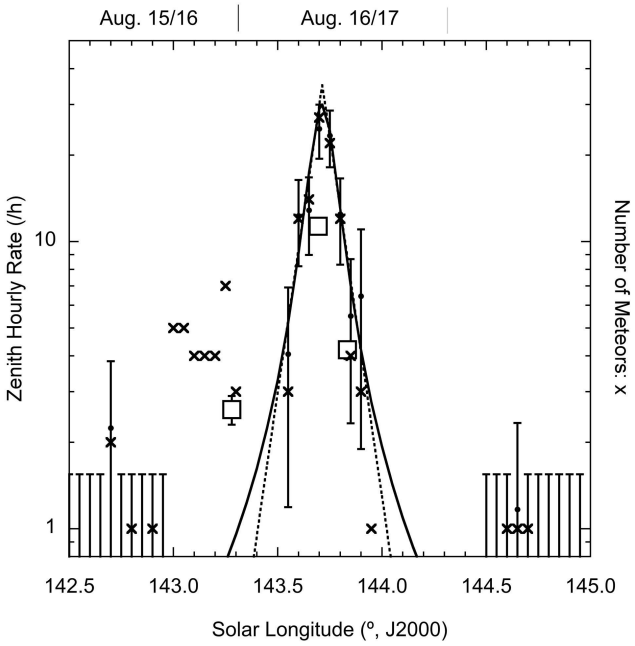

Figure 4 – Counts per bin (x) and Zenith Hourly Rates.

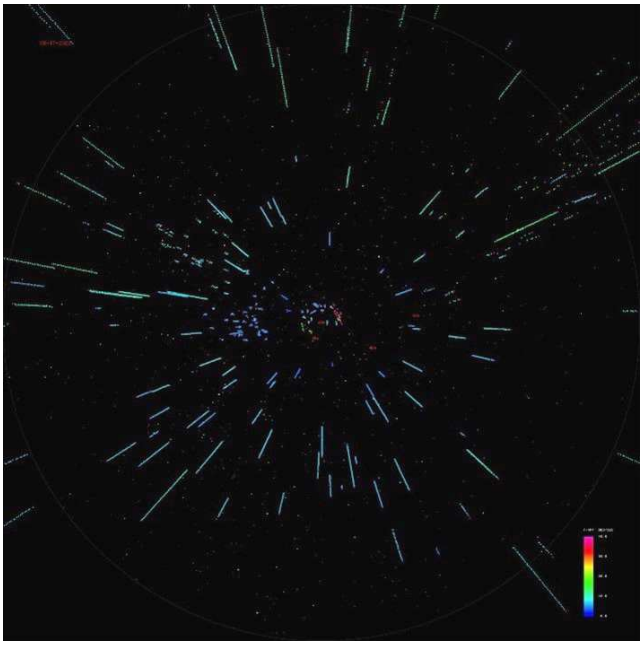

Figure 5 – Gnomic projected tracks 60° about the August delta-Capricornids radiant from Namibia in the night of 2022 August 16/17.

than 2 cm in size, suggesting some fragmentation may have occurred since ejection from the comet.

Figure 4 shows the activity curve. The shower meteors were counted and binned in $0\overset{\circ}{.}05$ ($\sim$ 1 h) intervals of solar longitude, and those counts from all stations combined are plotted as crosses. A number of CAMS networks detected small numbers of meteors in the solar longitude interval $143\overset{\circ}{.}0 - -143\overset{\circ}{.}3$ (first peak), while CAMS Namibia detected the main peak (second peak).

Those counts were corrected to Zenith Hourly Rates for the observations made in Namibia. Conditions in Namibia were excellent, with the radiant at 33° in the beginning of the night, rising to 80° around midnight and dropping below 30° elevation only in the last two hours of the night. The survey area monitored by the cameras (with camera fields of view above 30° elevation at a given site) was similar to the area covered by a standard visual observer, taken to be above 32° elevation (Jenniskens, 1994). Over that area, the number of meteors detected ($\Sigma P(m)\chi^m$) by a visual observer would be only 40% more than the number of meteors triangulated by the video cameras for the magnitude size distribution index of $\chi = 2.2$.

An exponential curve fitted to the activity (e.g., Jenniskens, 1994) gives a peak rate of ZHR = 35 and a B-slope parameter of $B = -5.0 \pm 0.5$ (dashed line in Figure 4). A Lorentz curve fitted to the data gives a peak rate of ZHR $\sim$ 30 and a Full-Width-at-Half-Maximum of $0\overset{\circ}{.}15$. This duration is related to the outflow conditions during ejection. Both solutions are centered on solar longitude $143\overset{\circ}{.}714 \pm 0\overset{\circ}{.}005$, which corresponds to 2022 August 16, $22^{\rm h}13^{\rm m}$ UTC.

The resulting ZHR values are slightly higher than those derived from Global Meteor Network observations at `https://globalmeteornetwork.org/flux/plots/flux_oADC2022_sol%3D143.00-144.50_year_2022_full.png`, shown by open squares in Figure 4.

The early August 15/16 observations (Peak 1) that first alerted us to the outburst were made mostly by the CAMS Chile (network #16), LO-CAMS (#6), and CAMS California (#1) networks. This activity may be part of a more extended activity that also produced some meteors earlier and later than the main peak. Because several networks were involved with different observing conditions, that activity is difficult to quantify.

The observed radiant during the main Peak 2 was R.A. = 325.28 ± 0.06, Decl. = -11.40 ± 0.06, and $V_g = 24.12 \pm 0.14$ km/s, with errors here describing the accuracy of determining the median value, not the dispersion in the values as are listed in Tables 1 and 2.

4 Discussion

The outburst was detected not only among triangulated meteors, but also in the single-station meteors. Figure 5 shows those meteors detected by CAMS Namibia that radiated from the August delta-Capricornids radiant.

The observed solar longitude of $143\overset{\circ}{.}714$ of the peak is close to that predicted ($143\overset{\circ}{.}772$), about 1.5 h earlier. The FWHM of the shower is $0\overset{\circ}{.}15$, which corresponds to about 3.6 h, so that the prediction was in good agreement with the observations. The predicted radiant was given as R.A. = $326\overset{\circ}{.}8$, Decl. = $-15\overset{\circ}{.}1$, while the observed radiant was only $+1\overset{\circ}{.}5$ different in R.A. and $+3\overset{\circ}{.}7$ in Decl., close considering the low inclination of the orbit and strong rotation of the nodal line.

The initial confusion about the outburst identity was due in part to the big difference in the orientation of the nodal line for the orbit of 45P compared to that of the meteoroids. 45P had an argument of perihelion of $326\overset{\circ}{.}3$ and node $88\overset{\circ}{.}9$ in the 2017-Aug-10 Epoch, which adds up to a longitude of perihelion of $55\overset{\circ}{.}3$. In

Table 1 – Radiant and orbital elements of the observed August delta-Capricornids. N# is the network number (Jenniskens, 2023).

#	$\lambda_\odot$ (°)	R.A.$_g$ (°)	Decl.$_g$ (°)	V_g (km/s)	q (AU)	a (AU)	e	i (°)	ω (°)	Node (°)	Mv	N#
1	142.6911	327.40	−14.94	24.66	0.521	2.86	0.818	1.45	94.6	322.63	3.3	17
2	142.7164	320.88	−13.43	23.00	0.605	3.42	0.823	1.32	263.7	142.78	1.5	17
3	142.8027	324.12	−11.96	24.03	0.554	3.08	0.820	1.77	270.2	142.83	1.8	8
	Peak 1:											
4	142.9142	325.30	−8.39	23.20	0.539	2.34	0.770	4.18	274.3	142.93	−1.4	16
5	143.0102	324.44	−12.10	23.67	0.557	2.90	0.808	1.55	270.2	143.14	−2.0	19
6	143.0144	323.80	−9.50	22.64	0.567	2.46	0.770	3.54	270.6	143.03	0.7	16
7	143.0158	322.82	−14.60	21.57	0.606	2.52	0.760	0.05	262.4	146.65	−1.6	14
8	143.0205	324.43	−11.28	24.38	0.548	3.20	0.829	2.25	270.7	143.10	−2.2	2
9	143.0220	323.42	−11.40	27.16	0.534	8.44	0.937	2.66	268.7	143.04	−1.7	16
10	143.0447	324.09	−9.48	25.00	0.540	3.51	0.846	3.86	271.0	143.09	−3.9	19
11	143.0494	324.55	−11.98	24.18	0.551	3.13	0.824	1.65	270.4	143.16	−1.4	2
12	143.0691	324.68	−11.93	23.86	0.553	2.94	0.812	1.65	270.7	143.18	−3.5	2
13	143.0693	327.50	−12.93	22.72	0.537	2.17	0.753	0.14	274.1	144.43	−0.9	14
14	143.0717	324.64	−13.06	24.97	0.546	3.74	0.854	0.83	269.9	143.12	−4.6	16
15	143.0870	324.20	−9.99	24.25	0.548	3.09	0.822	3.31	270.9	143.14	−1.0	19
16	143.1100	322.65	−15.84	22.67	0.602	3.11	0.807	0.77	85.0	322.86	−3.1	6
17	143.1143	324.52	−11.42	26.82	0.625	5.95	0.912	2.33	270.5	143.20	−2.9	1
18	143.1241	325.75	−11.01	25.11	0.525	3.26	0.839	2.22	273.1	143.20	−0.3	2
19	143.1479	324.75	−10.99	28.84	0.503	19.3	0.975	2.84	271.0	143.21	−1.5	6
20	143.1580	325.03	−10.81	24.41	0.540	3.06	0.823	2.49	271.8	143.23	−3.0	6
21	143.1616	322.70	−10.74	23.66	0.575	3.24	0.822	2.97	267.5	143.22	−0.6	6
22	143.1656	327.28	−15.53	23.48	0.543	2.56	0.788	1.79	93.1	323.06	−3.0	1
23	143.2025	325.06	−11.43	27.75	0.511	8.09	0.937	2.25	271.3	143.28	−2.2	6
24	143.2071	323.92	−11.77	24.05	0.561	3.25	0.827	1.96	269.1	143.27	−0.2	2
25	143.2217	321.03	−8.76	29.89	0.536	∞	1.063	5.96	265.0	143.25	−3.4	1
26	143.2242	324.82	−11.47	23.96	0.551	2.95	0.813	1.97	271.0	143.22	−2.4	16
27	143.2253	325.70	−12.10	27.17	0.511	5.86	0.913	1.44	272.2	143.22	−1.5	16
28	143.2386	324.20	−8.40	29.74	0.496	∞	1.000	5.60	271.1	143.27	−0.7	6
29	143.2412	325.45	−11.91	26.92	0.516	5.55	0.907	1.66	271.8	143.24	−2.0	16
30	143.2595	325.00	−11.44	23.99	0.548	2.93	0.813	1.95	271.2	143.34	−3.0	6
31	143.2612	324.74	−13.47	25.94	0.540	4.93	0.891	0.48	269.2	143.58	−2.7	6
32	143.2615	324.27	−13.62	24.31	0.561	3.52	0.840	0.45	268.3	143.59	−5.1	6
33	143.2727	324.91	−11.44	25.26	0.537	3.75	0.857	2.08	271.0	143.35	−2.8	1
34	143.2811	324.86	−11.62	23.85	0.552	2.92	0.811	1.84	270.8	143.37	−1.9	1
35	143.3065	324.85	−11.64	23.85	0.553	2.93	0.811	1.82	270.7	143.39	−3.6	1
36	143.3079	324.77	−11.64	23.99	0.552	3.01	0.817	1.85	270.6	143.39	−2.2	1
<>	143.16	324.7	−11.5	24.3	0.546	3.20	0.823	2.0	270.7	143.22		
σ	±0.10	±1.2	±1.7	±2.0	±0.024	±0.071	±1.3	±2.5	±0.65			

contrast, the meteors had a quite different argument of perihelion of 270.°9 and a node 143.°8, which adds up to about the same longitude of perihelion of 54.°7. So, the ellipse is oriented in the same direction in space, but the nodal line has rotated. The difference in orientation of the nodal line of the current orbit is mostly a consequence of a close encounter of the comet with Jupiter in 1983 (Jenniskens, 2023).

The earlier encounters predicted by Maslov came with caveats. The 2019 prediction was thought to produce mostly faint meteors and at a ZHR less than 10. We checked the available video data and confirm that no detection was made (Figure 6). Several networks were observing at the time of the encounter, but only two meteors (not related to this shower) were detected in this general area on November 6 between 02^h30^m and 04^h30^m UTC. Although the predicted 2019 encounter is almost three months later than our observed 2022 shower, this is consistent with a comet at low orbital inclination.

The shower was initially given the designation M2022-Q1 by the Meteor Data Center, this being the first example following the introduction of shower designations by the IAU Commission F1 in 2022. Designations are temporary markers, with the assignment of number, code and name being postponed to the future. In this case, the shower was quickly found to already be in the list, and the designation was removed from the list. However, that may not be appropriate, because the shower is now also known in the literature by that designation. A later assignment of shower names will automatically create a duplication of the list.

Table 2 – Partial list (every 3rd of 98 total) of observed second peak August delta-Capricornids.

#	$\lambda_\odot$ (°)	R.A.$_g$ (°)	Decl.$_g$ (°)	V_g (km/s)	q (AU)	a (AU)	e	i (°)	ω (°)	Node (°)	Mv	N#
	Peak 2:											
37	143.5633	325.20	−11.45	24.09	0.549	3.02	0.818	1.90	271.0	143.61	−1.4	17
40	143.5836	327.02	−11.25	23.44	0.534	3.42	0.779	1.57	274.5	143.64	2.0	17
43	143.5962	328.18	−10.56	23.88	0.513	2.34	0.781	1.86	277.1	143.64	−0.3	8
46	143.6111	324.81	−11.54	25.85	0.537	4.58	0.883	2.06	270.1	143.65	0.5	17
49	143.6185	325.41	−11.30	24.00	0.548	2.93	0.813	1.96	271.4	143.66	3.3	8
52	143.6252	324.15	−10.84	28.15	0.522	15.9	0.967	3.05	269.1	143.65	−2.1	17
55	143.6444	324.60	−11.65	25.18	0.547	4.00	0.863	1.97	269.5	143.69	2.6	17
58	143.6593	324.30	−11.26	23.68	0.564	3.03	0.814	2.21	269.2	143.76	0.2	3
61	143.6642	326.36	−11.43	24.79	0.529	3.12	0.830	1.68	272.9	143.71	2.8	17
64	143.6671	325.13	−11.03	23.73	0.553	2.85	0.806	2.20	270.9	143.70	2.9	17
67	143.6790	325.81	−11.78	28.92	0.499	19.5	0.974	1.79	271.5	143.72	1.8	17
70	143.6807	325.06	−11.49	25.63	0.537	4.23	0.873	2.02	270.4	143.72	2.2	17
73	143.6898	326.06	−11.55	23.69	0.545	2.70	0.798	1.58	272.3	143.74	0.9	17
76	143.6948	325.38	−11.41	23.84	0.551	2.89	0.809	1.87	271.1	143.73	0.9	17
79	143.6980	325.56	−11.19	24.11	0.545	2.95	0.815	2.02	271.5	143.74	0.2	17
82	143.7026	325.28	−11.54	23.72	0.554	2.86	0.807	1.78	270.8	143.74	3.0	17
85	143.7049	325.14	−11.53	27.78	0.517	9.40	0.945	2.13	270.4	143.74	0.4	17
88	143.7170	324.95	−11.53	26.98	0.526	6.64	0.921	2.12	270.1	143.75	1.3	17
91	143.7223	325.27	−11.19	24.17	0.548	3.06	0.821	2.09	271.0	143.76	0.6	17
94	143.7273	324.46	−11.25	28.25	0.520	17.2	0.970	2.60	269.3	143.76	−3.6	17
97	143.7305	325.08	−9.67	23.20	0.556	2.58	0.785	3.20	271.5	143.75	0.3	17
100	143.7371	324.87	−11.60	23.58	0.561	2.90	0.807	1.81	270.0	143.77	2.9	17
103	143.7403	325.32	−11.23	24.20	0.548	3.07	0.821	2.05	271.0	143.77	2.0	17
106	143.7591	326.94	−11.24	23.55	0.536	2.49	0.785	1.59	274.0	143.80	2.4	16
109	143.7658	325.41	−12.22	23.72	0.555	2.90	0.809	1.22	270.5	143.82	1.4	16
112	143.7711	325.73	−11.63	24.73	0.539	3.31	0.837	1.67	271.4	143.80	1.5	17
115	143.7789	325.45	−10.99	23.51	0.553	2.72	0.797	2.14	271.3	143.81	1.8	17
118	143.7968	325.34	−11.11	24.26	0.547	3.10	0.824	2.14	271.0	143.82	2.7	17
121	143.8015	325.22	−11.40	23.88	0.554	2.96	0.813	1.91	270.6	143.84	1.5	16
124	143.8069	324.51	−10.43	23.65	0.561	2.94	0.809	2.79	269.8	143.82	1.9	17
127	143.8297	325.35	−11.82	26.39	0.530	5.22	0.899	1.72	270.4	143.85	2.2	17
130	143.8596	325.29	−12.35	27.24	0.525	7.59	0.931	1.32	269.9	143.88	2.9	17
133	143.8964	326.23	−11.01	24.14	0.539	2.86	0.811	2.00	272.5	143.91	1.2	17
134	143.9281	325.55	−11.51	23.59	0.555	2.80	0.802	1.73	270.9	143.93	2.4	17
<>	281.17	325.3	−11.4	24.1	0.546	2.99	0.814	1.96	270.9	143.75		
σ	±0.16	±0.8	±0.5	±1.4	±0.015	±0.059	±0.42	±1.6	±0.08			
135	144.6041	328.05	−9.54	23.38	0.529	2.32	0.772	2.61	275.4	144.67	−0.5	7
136	144.6475	324.85	−9.59	24.20	0.559	3.30	0.831	3.40	269.2	144.67	0.2	17
137	144.7198	326.92	−10.32	23.93	0.541	2.76	0.804	2.33	272.5	144.81	−0.7	5

5 Conclusions

For the first time, meteors have been observed that are demonstrated conclusively to have originated from comet 45P/Honda-Mrkos-Pajdušáková. The predicted 1980-dust trail encounter by Maslov (2020) is in good agreement with the observations, suggesting other such predictions for this comet may also come to fruition in the future.

The meteoroids were cm-sized, but perhaps smaller than material ejected by the comet, suggesting fragmentation. However, the observation of debris ejected in the 1980 return in 2022 demonstrates that some material survives the interplanetary medium over this timescale and makes it more likely that even older meteoroids previously linked to 45P may in fact have originated from this comet.

Acknowledgements

We thank the CAMS network and station operators for their efforts in building and maintaining CAMS. This work was supported by NASA grants 80NSSC 19K0563 (Solar System Workings) and 80NSSC19K0513 (Emerging Worlds) to PJ. The CAMS expansion in the southern hemisphere was made possible by the University of Arizona in support of the OSIRIS-REx mission, based upon work supported by NASA under Contract NNM10A11C issued through the New Frontiers Program.

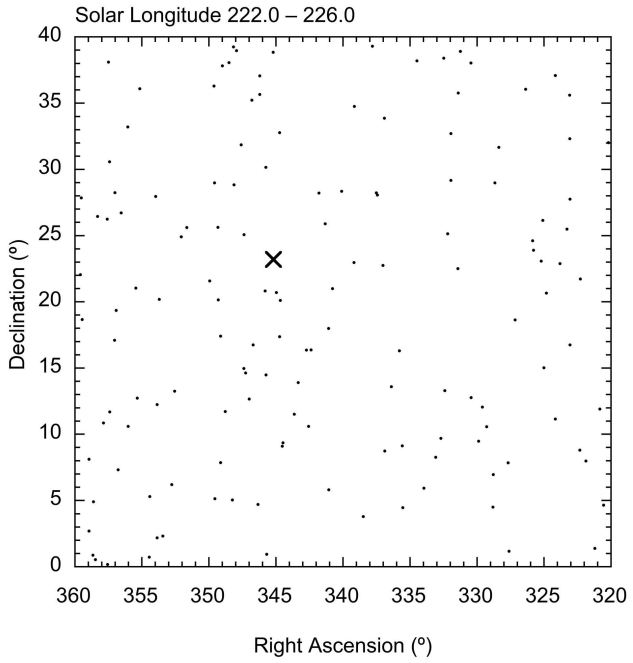

Figure 6 – Predicted 2019 encounter (x). Dots represent detected meteors within the two hour window on November 6 2019, $02^{h}30^{m}$–$04^{h}30^{m}$ UTC corresponding to Maslov's prediction.

References

Combi M. R., Mäkinen T., Bertaux J. L., Quémerais E., Ferron S., and Coronel R. (2020). "Comet 41P/Tuttle-Giacobini-Kresak, 45P/Honda-Mrkos-Pajdusakova, and 46P/Wirtanen: Water Production Activity over 21 yr with SOHO/SWAN". *The Planetary Science Journal*, **1:3**, 72. 7 pp.

Jenniskens P. (1994). "Meteor stream activity I. The annual streams". *Astronomy and Astrophysics*, **287**, 990–1013.

Jenniskens P. (2006). *Meteor Showers and their Parent Comets*. Cambridge University Press, Cambridge, UK. 790 pp.

Jenniskens P. (2022a). "18-Aquariid meteor shower 2022". *CBET*, **5159**. (published 2022, August 17), Ed.: D. W. E. Green. Cambridge: Central Bureau for Astronomical Telegrams.).

Jenniskens P. (2022b). "August delta Capricornids meteor shower 2022". *eMeteorNews*, **7:5**, 306.

Jenniskens P. (2023). *Atlas of Earth's Meteor Showers*. Elsevier, Amsterdam, 824 pp pages.

Maslov M. (2020). "45P-ids 2022: prediction of activity". `http://feraj.ru/Radiants/Predictions/45p-ids2022eng.html` . (last accessed August 19, 2022).

Porubcan V. and Gavajdova M. (1994). "A search for fireball streams among photographic meteors". *Planetary and Space Science*, **42:2**, 151–155.

Roggemans P., Šegon D., Vida D., Greaves J., Sekiguchi T., Angelsky A., and Davydov A. (2022). "Near anti-helion meteor shower outburst recorded by Global Meteor Network". *eMeteorNews*, **7:5**, 293–301.

Sekiguchi T. (2022). "New radiant on Aquarius/Capricorn border by the SonotaCo Network". *eMeteorNews*, **7:5**, 302–303.

Springmann A., Harris W. M., Ryan E. L., Lejoly C., Howell E. S., Mueller B. E. A., Samarasinha N. H., Woodney L. M., and Steckloff J. K. (2022). "Repeating Gas Ejection Events from Comet 45P/Honda-Mrkos-Pajdušáková". *The Planetary Science Journal*, **3:1**, 15.

Springmann A., Howell E. S., Harmon J. K., Lejoly C., Rivera-Valentin E. G., Virkki A., Zambrano-Marin L. F., Taylor P. A., Harris W. M., Mueller B. E. A., Samarasinha N. H., and Rodriguez Sanchez-Vahamonde C. (2017). "Particle Sizes in the Coma of Comet 45P/Honda-Mrkos-Pajdušáková from Arecibo Radar Observations". In *AAS/Division for Planetary Sciences Meeting Abstracts #49*, volume 49 of *AAS/Division for Planetary Sciences Meeting Abstracts*. page 305.06.

Terentjeva A. K. (1989). "Fireball streams.". *WGN, Journal of the International Meteor Organization*, **17:6**, 242–245.

Vaubaillon J. and Christou A. A. (2006). "Encounters of the dust trails of comet 45P/Honda-Mrkos-Pajdusakova with Venus in 2006". *Astronomy and Astrophysics*, **451:2**, L5–L8.

Handling Editor: Javor Kac

Comparison of three different camera systems monitoring the meteor activity over Hungary in 2020–2023

Lívia Deme, Krisztián Sárneczky, Antal Igaz, Balázs Csák, Nándor Opitz, Nóra Egei, and József Vinkó [1]

We present statistical analysis of visual meteor data taken with networks of meteor cameras operating in Hungary between 2020 and 2023. We use three different camera systems: a set of traditional MetRec-based video cameras, a self-developed automated DSLR camera system and a network of newly installed AllSky7 camera stations. Similarities and differences between the data produced by the three systems, aimed at recording different types of meteor phenomena, are presented and discussed.

Received 2023 December 19

1 Introduction

Dust grains from cometary tails and/or ejected asteroid material, ranging from several microns to roughly meter-sized bodies in diameter, are responsible for most of the observed meteor events when entering Earth's atmosphere (see e.g. Ye and Jenniskens, 2022, and references therein). Meteor populations are usually divided into two basic categories: sporadic meteors having no preferred direction, i.e. they appear at random positions on the sky all year round, and meteor showers arriving from a specific direction, called the radiant. Meteoroid orbits causing many of the currently known meteor showers can be traced back to a parent body, usually a comet or an asteroid (McIntosh, 1991; Jenniskens, 1994; Ye & Jenniskens, 2022). Sporadic meteors are thought to be originated from old cometary tails and/or interplanetary dust trails that have been dissolved since their ejection, providing a more-or-less stationary background of incoming sporadic meteor flux.

Since the visual meteor activity, i.e. the hourly or nightly rate of observable meteors are usually increased by more than an order of magnitude during the peak date of showers, meteor showers have been studied more frequently in the literature. Still, there is an increasing number of papers dealing with the statistical properties of sporadic meteors (see e.g. Jones and Brown, 1993; Rendtel, 2006; Wiegert et al., 2009; Dubietis and Arlt, 2010, and references therein).

Despite the lack of a specific radiant, several preferred directions of sporadic meteors can be identified (e.g. Campbell-Brown and Jones, 2006): most of the sporadic meteors arrive from the apex of Earth's orbit, while the helion and antihelion sources are located in the ecliptic roughly perpendicular to the apex-antapex direction. Beside these sources, two additional ones at $\sim$ 60 degrees north and south of the ecliptic, named northern and southern toroidal sources, were identified from radar observations (Jones & Brown, 1993). The apex and the antihelion sources provide the majority of the visually observable sporaric meteor population (Rendtel, 2006).

[1]HUN-REN Research Centre for Astronomy and Earth Sciences, Konkoly Observatory, Konkoly Thege út 15-17, Budapest, 1121 Hungary. Email: vinko@konkoly.hu

IMO bibcode WGN-516-deme-comparison
NASA-ADS bibcode 2023JIMO...51..166D

In this paper we use data from different meteor camera systems operating in Hungary to reveal the visual meteor activity between 2020 and 2023. Here we concentrate on the statistical properties of sporadic meteors and the brightest events, mostly fireballs. The measured properties of recent meteor showers will be presented in a subsequent paper. In the next section we briefly summarize the technical parameters of the camera systems applied in this study, followed by the description of the data taken by the different cameras, the obtained results and our conclusions.

2 Meteor camera systems in Hungary

In Hungary, the deployment of video camera systems for automated detection of visual meteors was started more than 20 years ago. Most of those cameras are still operating. They consist of an analogue video camera (either PAL, or NTSC) attached to a PC having a Matrox frame-grabber video card that samples the analogue video stream, and takes rapid snapshots of digital frames ($\sim$ 25 frames per second) when a moving object, presumably a meteor, appears in the field-of-view. Meteor detection and measurement is handled by the "Meteor Recognizer" (MetRec, `https://metrec.org`) software. The sensitivity limit is typically between 4 and 5 magnitude, depending on the type and manufacturer of the particular camera. These cameras are integrated within the camera network of the International Meteor Organization (IMO). In this paper we use three of them: `Hukon`, `Hupis` and `Huhod`. The basic parameters for these three cameras are summarized in Table 1. MetRec uses a well-defined set of reference stars for computing astrometry and calibrated photometry for each meteor event.

More recently, starting in 2017, our team at Konkoly Observatory developed and installed a new system, named Konkoly Meteor Observatory Network (KoMON), which is based on a combination of a digital video camera with a more modern DSLR digital camera. The moving object is recognized by the video camera uses a custom Python-based software then it triggers the DSLR camera to take digital frames for 10 seconds. An LCD panel, placed in front of the CMOS chip of the DSLR camera, chops the incoming light by a pre-programmed de Bruijn sequence (Howie et al., 2017) to separate the likely meteors from other, slow-moving objects (airplanes, birds, treeleafs, insects, satellites, etc).

Table 1 – Parameters of the MetRec-based video cameras

Name	Longitude (deg.)	Latitude (deg.)	Altitude (m)	Center Az (deg.)	Center Alt (deg.)	Field-of-view (deg. × deg.)
HUKON	18.963793	47.499622	490	317.7	40.9	80.7 × 56.4
HUPIS	19.895140	47.917229	947	348.1	50.8	80.9 × 56.8
HUHOD	20.312500	46.418499	79	328.7	50.8	80.3 × 55.8

Table 2 – Camera parameters for the KoMON stations

Site name	Longitude (deg.)	Latitude (deg.)	Altitude (m)	Direction	Field-of-view (deg. × deg.)
Konkoly	18.963793	47.499622	490	W	90 × 80
Piszkesteto	19.895140	47.917229	947	Z,N,E,S,W	360 × 90
Gothard	16.6031	47.2578	232	Z,N,E,S	270 × 90
Devavanya	20.9356	47.0814	84	Z,N,E,S,W	360 × 90
Becsehely	16.7918	46.4479	180	Z,N,E	180 × 90

Table 3 – Camera parameters for the AllSky7 stations

Site name	Camera name	Longitude (deg.)	Latitude (deg.)	Altitude (m)	Field-of-view
Konkoly	AMS18	18.963793	47.499622	490	All-sky
Becsehely	AMS71	16.7918	46.4479	180	All-sky
Piszkesteto	AMS72	19.895140	47.917229	947	All-sky
Fehergyarmat	AMS97	22.5178	47.9854	111	All-sky
Hortobagy	AMS98	21.1451	47.5941	121	All-sky

The KoMON system has been designed to be sensitive to the brightest, relatively slow meteors, like fireballs. Such meteors might be missed by the conventional video camera systems, because they might saturate the camera causing a failure of the recognition algorithm. Thus, the KoMON system detects only the brightest end of the meteor brightness distribution function (BDF), and, by design, it likely detects the slower events instead of the fastest ones. The system parameters are collected in Table 2.

At the time of writing this paper, proper astrometry and photometry is not yet implemented for the KoMON system. Thus, the cameras in the KoMON network are capable of recording only the moment (within ~ 1 second) of the beginning of a meteor event and its angular speed along the projected trajectory. An integrated digital image (taken with 10 seconds exposure time) as well as digital video frames are also stored for each triggered event. Due to the lack of calibrated digital photometry, we were only able to use a visual brightness estimate for the recorded meteors that appeared brighter than the stars on the corresponding digital frame. This way we can still classify meteors that are brighter than ~ 0 visual magnitude, beside the lack of more precise photometric information.

Finally, starting in mid-2021, several stations of the AllSky7 camera system (`https://allsky7.net`) have been deployed at various sites in Hungary. These stations consist of an integrated unit of 7 cameras providing practically all-sky coverage, calibrated astrometry and broad brightness sensitivity range. The average limiting magnitude for each unit is ~ 4 mag. The parameters for the stations that are at our group's disposal are summarized in Table 3.

3 Data

The three different camera systems provided different types of data for us. The most complete high-level dataset was obtained by the MetRec-based cameras, after post-processing and cleaning the nightly data by visual inspection. MetRec is able to classify each recorded meteor based on its projected trail on the sky. If a meteor trail is close to a radiant of a known meteor shower, and the meteor angular velocity matches to the known velocity of that meteor shower, then the meteor is classified as a member of that particular shower. The sporadic meteors belonging to the antihelion source are classified as `ANT`. Two other ecliptical showers, the Northern and Southern Taurids (`NTA` and `STA`, respectively) are also thought to belong to the sporadic meteor population. All other meteors that cannot be assigned to any meteor shower are classified by MetRec as SPO. Many of those meteors are coming roughly from the apex direction. We extracted and analyzed the following data from the logfile of each night: date, time (both in UT), classification and magnitude for each event. We also used the nightly statistics computed by the auxiliary program CheckLog: the total number of meteors, the number of sporadic meteors and the effective observing time for each recorded night. These numbers were then summed up for each month to create a monthly statistics from 2019 December to 2023 October.

The KoMON system provided a more limited dataset. We used only the UT dates and time for each

event recorded by each camera since 2019 December up to 2023 October. Simultaneous detections were treated as a single event, using a maximum time difference of ±1 second for multiple detections of the same meteor. We also visually inspected all frames to identify potential fireballs by selecting meteors that appeared brighter than any of the stellar objects on each frame (see Section 2). Finally, we corrected the number of detected meteors for the number of active cameras at each site, resulting in a number of detections per a single DSLR camera FoV on each observed night.

The AllSky7 system uses a custom Python-based software for meteor detection, astrometry and brightness estimates. Neither classification of meteor showers, nor calibrated photometry is done at the individual sites, though. The meteor shower classification is part of the server-based multi-station analysis of the AllSky7 datasets. Since the primary goal of the present study is meteor statistics, we extracted and used only the date and time of each event recorded by the AllSky7 stations at each site.

4 Results

In this section we describe our results based on the data obtained by the three camera systems.

4.1 The population index of sporadic meteors

Based on the magnitude information and classification for each meteor by MetRec, we were able to determine the nightly variation of the population index for the sporadic meteors, after summing up the number of events labeled as `SPO`, `ANT`, `NTA` or `STA`.

The population index is determined from the observed cumulative BDF for a sample of meteors:

$$N(m) = N_0 \cdot r^m \quad (m < m^*), \tag{1}$$

where m is the magnitude, $N(m)$ is the number of meteors brighter than m magnitude, N_0 is a normalization constant, m^* is the magnitude limit for detection completeness and r is the population index. From Equation (1) the population index can be derived simply as $r = N(m+1)/N(m)$ for $m < m^*$.

We adopted m^* as the magnitude of the peak of the meteor BDF histogram using 1 magnitude-wide bins, and derived the population index using the numbers for 2 magnitude bins below the peak. Figure 1 illustrates the methodology: the left panel shows the histogram of the BDF of all sporadic meteors from the `HUKON` camera, which turned out to be the most stable one from photometric point of view. The right panel plots the cumulative BDF for the same dataset. $m^* = 1$ is estimated as the magnitude of the maximum of the BDF in the left panel. The blue line is a least-squares fit of Equation (1) to the points within the interval of $[m^* - 2 < m < m^*]$.

Figure 2 shows the variation of the nightly population indices for the three MetRec cameras as a function of Julian dates. Ignoring the few outliers (probably due to low number of recorded meteors and/or inferior weather conditons), most of the indices are within the

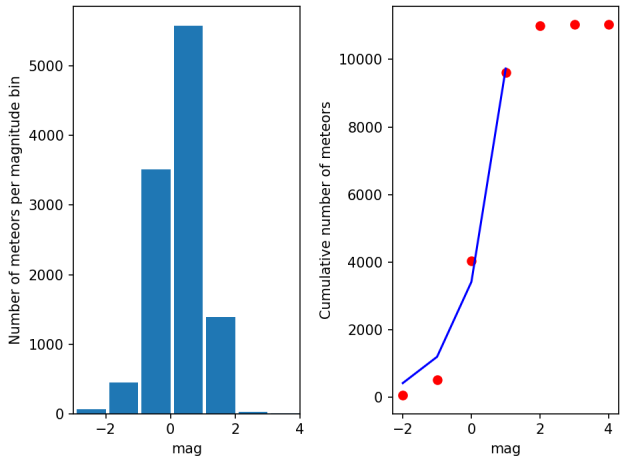

Figure 1 – The method used for population index determination. Left panel: the observed number of meteors ($n(m)$) as a function of magnitude. Right panel: the cumulative BDF ($N(m)$) against magnitude. The blue line indicates the fitted model from Equation 1.

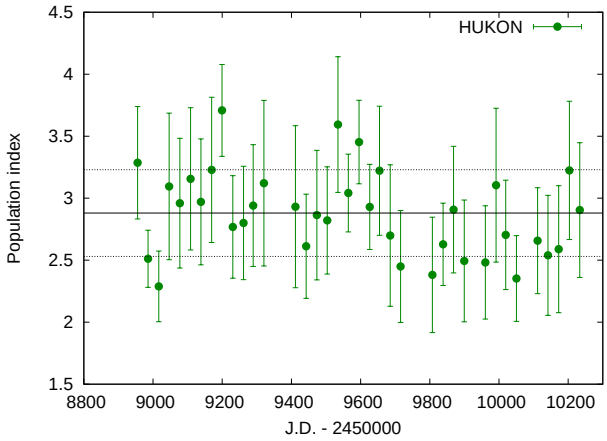

Figure 2 – The variation of the nightly population index of `SPO` meteors recorded by `HUKON` during 2020–2023.

range of $2 < r < 4$. The black horizontal line indicates the mean value of $\langle r \rangle = 2.85 \pm 0.48$ for the combined sample of the three cameras. This is in good agreement with result of Rendtel (2006) who obtained $\langle r \rangle = 2.95 \pm 0.15$ as a yearly average.

Note, however, that the population index determination suffers from known issues. For example, Molau (2015) discussed several improvements which may result in somewhat different population indices for the same dataset. He obtained $\langle r \rangle \approx 2.5$ as a mean value for sporadic meteors, which is very similar to the results of Jenniskens (1994) (2.2 – 2.5) and Vida et al. (2020) ($\langle r \rangle = 2.55 \pm 0.06$). More recently Betzler (2023) suggested a different statistical function (the q-exponential function) to represent the cumulative meteor BDF. He obtained $\langle r \rangle = 3.63 \pm 0.01$ based on a more extended magnitude range of $-5 < m < 0$. The differences between these reported population indices illustrate that despite the improvement of the methodology, these estimates may still suffer some sort of systematic errors. Nevertheless, in the following we apply our results above, $\langle r \rangle = 2.85 \pm 0.48$ for consistency. Contrary to Betzler (2023), we did not detect significant variation in the

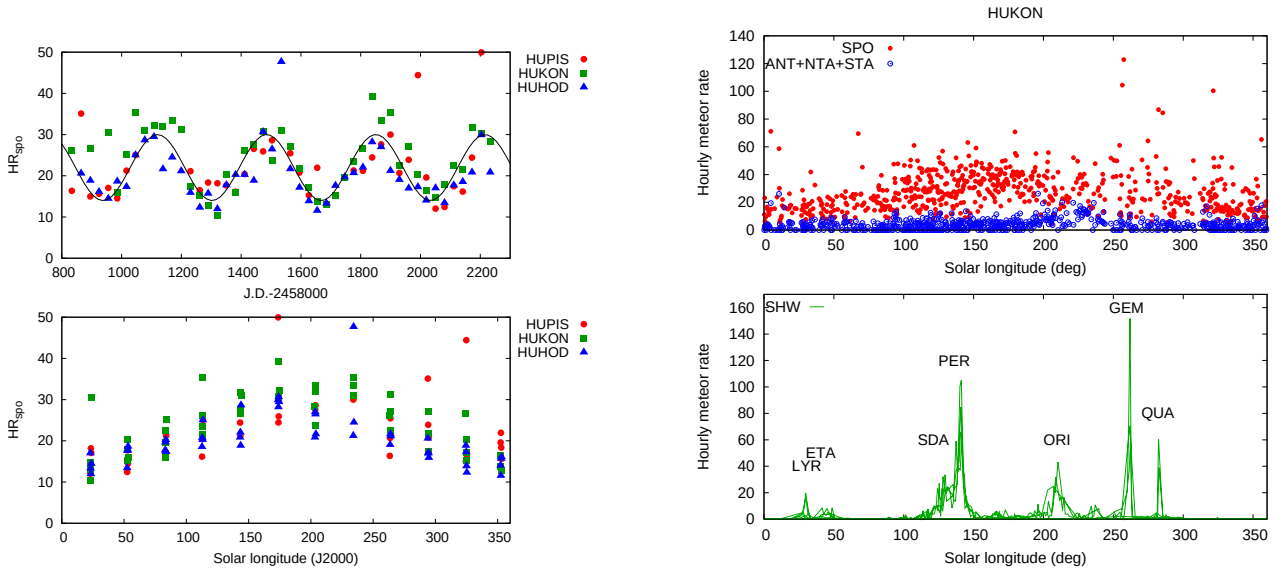

Figure 3 – Left: The hourly rates of `SPO` meteors as a function of J.D. (upper panel) and solar longitude (lower panel). Right: Hourly meteor rates by `HUKON` for all sporadic meteors, including `SPO`, `ANT`, `NTA` and `STA` (upper panel) and meteor showers (lower panel). Major showers are labeled by their IMO codes.

population index of sporadic meteors along a year (Figure 2).

4.2 The hourly rate of sporadic meteors

The rates of sporadic meteors were estimated from the `HUKON`, `HUPIS` and `HUHOD` data in the following way. We adopt the sporadic hourly rate (HR_{spo}) definition from Dubietis and Arlt (2010) as

$$HR_{spo} = \frac{n_{spo}}{t_{eff}} \cdot F \cdot r^{\Delta m}, \qquad (2)$$

where n_{spo} is the number of sporadic meteors per night, r is the population index, Δm is the magnitude difference between the camera sensitivity limit and a reference value, t_{eff} is the effective observation time in hours and F is the correction factor between the camera field-of-view (FoV) and that of a human observer. For the latter we adopt a conservative estimate that a human observer sees $\sim 1/3$ of the visible hemisphere of the sky. From Equation 2 it is seen that we do not correct the rate for the zenith distance of a fiducial "radiant" of sporadic meteors, unlike e.g. Rendtel (2006). It is a common practice to define $\Delta m = 6.5 - Lm$, where Lm is the limiting magnitude (the sensitivity limit) for a particular camera (Jenniskens, 1994).

We adopted the following nominal limiting magnitudes: $Lm = 4.5$ (`HUKON` and `HUPIS`) and $Lm = 4.0$ (`HUHOD`). Since these limiting magnitudes may change during the night due to variable weather conditions, we also attempted to use the nightly averaged values from the `.mag` files provided by MetRec. The limiting magnitude estimates by MetRec have a 1 minute resolution, thus, they could be used to model the variable weather conditions during each night. However, it was found that while using a variable Δm based on these data the night-to-night scattering of the calculated HR_{spo} values increases by a large amount, which is not physically expected for the true rate of sporadic meteors. Therefore, we decided to apply a single Δm value for each camera as listed above.

Figure 3 shows the results. In the upper left panel we plot HR_{spo} for all three cameras against Julian days. The annual oscillation, noted previously by many observers (e.g. Campbell-Brown and Jones (2006); Rendtel (2006)) is evident from these data. Dubietis and Arlt (2010) even found correlation between HR_{spo} and the solar activity cycle. Our data do not cover ~ 20 years, which would be necessary to confirm the existence of a ~ 11 year-long cycle, but the annual variation is recovered consistently by all three cameras.

The lower left panel of Figure 3 displays the same data against solar longitude. Again, the increase of HR_{spo} during the Fall season (September – November) is visible each year. This is fully consistent with the results of Dubietis and Arlt (2010) who also found a ~ 50 percent increase of HR_{spo} in September with respect to the rate measured in April. This annual variation of HR_{spo} seems to be consistent with the seasonal visibility of the apex direction during the 2nd half of the night.

Rendtel (2006) attributed the annual variation of HR_{spo} he found in the IMO database (VMDB) to the polluting effect of misclassified shower meteors (see Figure 6 in Rendtel (2006)). We also tested this effect, but found that this is less significant in our data. In the upper right panel of Figure 3 we plot the nightly HR_{spo} derived from the `HUKON` data as a function of solar longitude. It is seen that the `SPO` meteors (plotted with red symbols) dominate the majority of sporadic events, and the increase of the sporadic activity within $\lambda_\odot = 100 - 200$ deg is mostly due to `SPO` meteors. The antihelion source (plotted with blue symbols) provides only a small fraction of the total sporadic rate, and the annual variation is less visible in those data.

The lower right panel displays the inferred rates for meteor showers. These are only approximate ZHRs as

they are not corrected for radiant position to keep consistency with the measurement of the sporadic rates, and they are used only for comparison. Indeed, the appearance of several of the richest showers can be easily identified, and they are labeled. Comparing the top right panel with the bottom right figure, it is seen that the increase of the sporadic rate is not generally due to the polluting effect of showers. For example, in the late August – late October season ($\lambda_\odot = 150 - 200$), when HR_{spo} is the highest in our data, the activity from showers was negligible, at least from 2020 to 2023. On the other hand, a pollution effect can be identified during the Geminids in mid-December, but this is localized to a single night during the shower maximum, around December 13. Thus, we conclude that the increase of HR_{spo} during September – November is real. It correlates well with the seasonal visibility of the apex direction where most of the sporadic meteors are coming from, but it might also be connected with some sort of enhancement in the distributions of meteoroid parameters (mass, particle size, velocity, spatial density, etc.) that contribute to the appearance of visually identified meteors, observed locally from the northern hemisphere (Dubietis & Arlt, 2010).

Regarding the median value of HR_{spo} and its standard deviation, we measure 26.3 ± 6.8, 32.1 ± 9.2 and 26.9 ± 9.1 for `HUPIS`, `HUKON` and `HUHOD`, respectively. For the combined sample it is 28.4 ± 8.4. These values are generally higher than those in recent literature: they are a factor of ~ 3 higher than the results of Dubietis and Arlt (2010) ($HR_{spo} \sim 10 \pm 2$ from data by visual observers), and still somewhat higher than the estimate by Rendtel (2006) based on video meteor observations ($HR_{spo} \sim 22 \pm 3$). Since HR_{spo} as defined in Equation 2 depends critically on the assumed FoV of a visual observer as well as the proper statistical accounting of the unobserved faint meteors, the difference between our results and that of Rendtel (2006) is not significant. Note that if we had corrected the camera FoV to the whole area of the full sky hemisphere (2π steradian) instead of the FoV of a human observer, then the calculated rates should have been scaled up to 3 times higher values, resulting in ~ 85 sporadic meteors/hour.

4.3 The frequency of slow fireballs as potential impactors

Fireballs are spectacular events representing the brightest end of the BDF of visual meteors. Traditionally, meteors brighter than Venus ($m < -4$ mag) are called fireballs. Most of them produce flares during or at the end of their visible path, but the definition is related only to the visual brightness (i.e. brighter than -4 magnitude) and not the occurrence of any flares. Since fireballs are the most probable impactors among meteors, there is significant interest in studying their frequency in any meteor stream.

The KoMON system, as mentioned in Section 2, was designed to capture mostly the brightest and relatively slow meteors, in order to detect potential impactors. Despite its limited capabilities, we were able to visually identify the brightest events (brighter than ~ 0 magnitude) by visually inspecting every recorded frame, starting from 2019 December up to 2023 October. The reason for extending the magnitude limit to 0 mag, instead of -4 mag, was twofold. First, since there is no calibrated photometry available in the KoMON system, only relative brightness estimates with respect to the brightest visible stars could be made. Second, since the real fireballs are rare, extending the magnitude limit from -4 mag down to 0 mag increases the number of events in the sample, thus, it becomes more suitable for statistical studies. In the following, when we refer to fireballs, we mean meteors brighter than 0 magnitude.

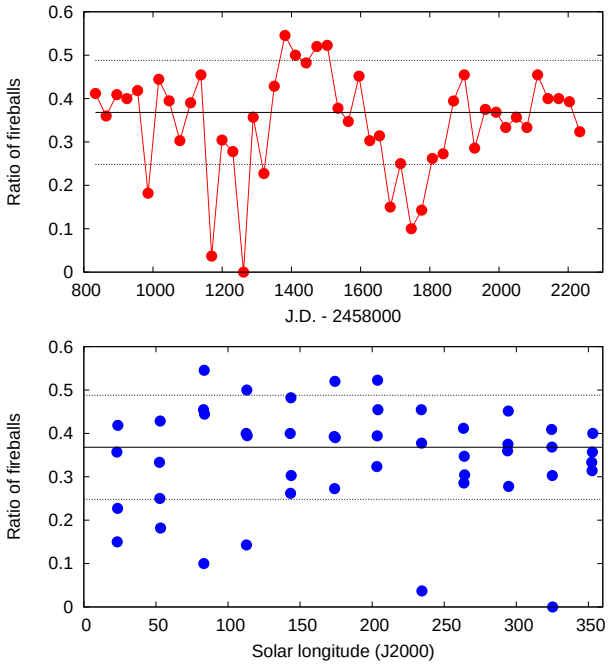

Figure 4 – The ratio of "fireballs" (meteors brighter than 0 mag in this paper) to the number of all meteors recorded by the KoMON system as a function of J.D. (top panel) and solar longitude (bottom panel)

Figure 4 plots the ratio of fireballs to all events recorded by the KoMON cameras as a function of Julian dates (upper panel) and solar longitude (lower panel). Meteor numbers belonging to the same month are summed, in order to get better statistics for these relatively rare events. Thus, each symbol represent the ratio of the monthly sum of fireballs to the sum of all recorded meteors. As mentioned in Section 2, multiple detections have been removed, thus, they do not introduce a bias in the number of fireballs. The mean fireball ratio for the whole sample turned out to be about 30 – 50 percent (0.37 ± 0.12). The actual numbers go below or above this range in a few months when very few meteors were detected by the KoMON cameras for a number of reasons (weather, technical issues, etc.).

Figure 5 displays the number of fireballs per month, normalized to a single camera and scaled up to all-sky FoV, again, as a function of J.D. (upper panel) and solar longitude (lower panel). These numbers can be regarded as the number of fireballs in each month for the whole sky above Hungary. Again, we used the monthly sums to reduce the fluctuations due to low

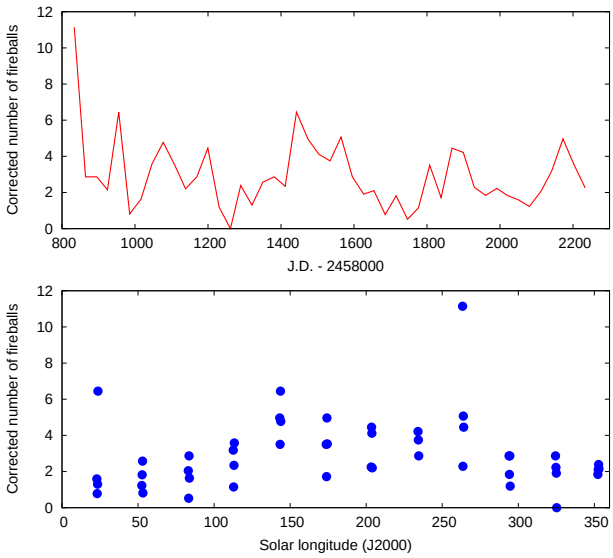

Figure 5 – The number of fireball events per month scaled up to all-sky as a function of J.D. (upper panel) and solar longitude (lower panel). The Geminids and Perseids are clearly identifiable as local maxima.

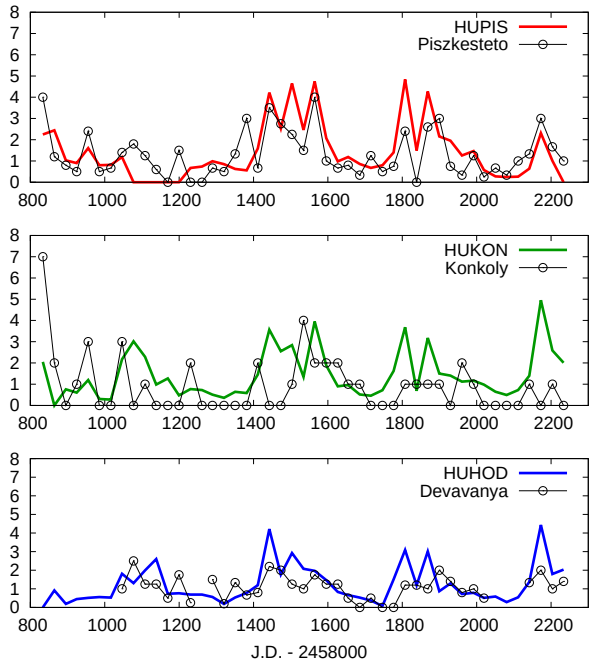

Figure 6 – The comparison of the KoMON fireball numbers normalized to a single camera (black lines with dots) and the MetRec monthly meteor numbers corrected for 0 magnitude (color curves). See text for explanation.

number statistics. As expected, meteor showers are clearly identifiable in these plots. For example, Geminids in 2019 December produced especially high number of fireballs. Later Perseids at $\lambda_\odot \sim 145$ deg showed the highest number of fireballs recorded by the KoMON system. The mean value is estimated as $N_{fb} = 2.94 \pm 1.91$ fireballs per month.

Finally, we compare the KoMON fireball numbers to the meteor numbers taken by the MetRec-based cameras after statistically selecting only the brightest meteors. Figure 6 shows the comparison for those cameras that are either at the same site (Piszkesteto – `HUPIS`,

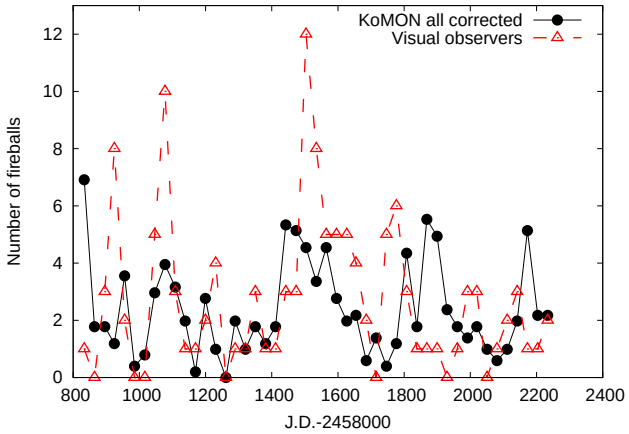

Figure 7 – The total number of KoMON fireballs corrected for the -4 magnitude limit (assuming a population index of $r = 1.5$, see text) plotted with filled red circles and the number of observed fireballs brighter than -4 magnitude reported by visual observers from Hungary (green open triangles).

Konkoly – `HUKON`) or relatively nearby (Devavanya – `HUHOD`). Since the camera FoV-s in the two systems are similar ($81° \times 56°$ for a MetRec camera and $90° \times 80°$ for a single KoMON camera), no correction for this factor was made. The KoMON data taken with multiple units at the same site were normalized to a single camera. The numbers from the MetRec-based cameras are corrected for the magnitude difference between the camera limiting magnitude and 0 mag, thus, applying the factor of $r^{\Delta m}$, where r is the population index. We found that if we set $r = 3.0$ and $\Delta m = -5.0$, -5.0 and -4.5 for `HUPIS`, `HUKON` and `HUHOD`, respectively, they give the best agreement between the MetRec and the KoMON data. It is seen in Figure 6 that the two datasets are generally consistent. Thus, the KoMON system is able to capture most of the meteors at the brightest tail of the meteor BDF if they appear within the camera field-of-view.

It is interesting how many true fireballs we can see if we use the original -4 mag limit as a cutoff. Using the same population index of $r = 3.0$, the normalized KoMON fireball numbers must be corrected with $r^{-4} \approx 0.012$. Such a correction would predict an average of ~ 0.036 fireball per month, i.e. a single fireball in every 2 years. This is clearly way below the actual number of detected fireballs, either by our cameras or by visual observers. Thus, the population index may be different from 3. This is expected because most of the true fireballs are due to shower meteors that have lower population index. Assuming $r = 1.5$ one would get the true fireball rate as ~ 0.6 per camera per month, which is a more reasonable estimate.

We have made an independent test in order to confirm this assumption by comparing the predicted number of KoMON fireballs brighter than -4 magnitude using the correction factor of r^{-4} with $r = 1.5$ with the number of actually observed fireballs brighter than -4 magnitude over Hungary. For the former we selected all fireballs detected by the KoMON system, while for the latter data we used the Hungarian mirror of the

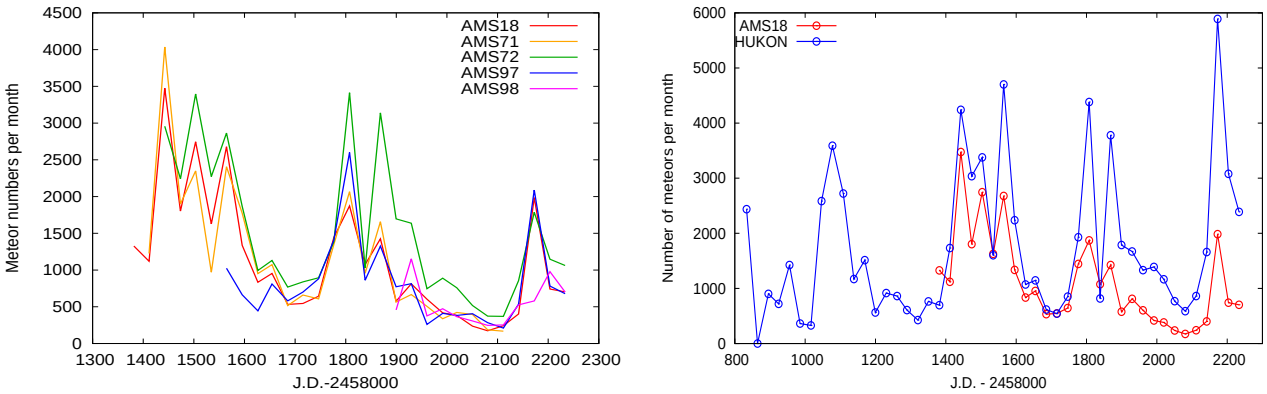

Figure 8 – Left panel: monthly meteor detections for the AllSky7 cameras. Right panel: comparison of monthly meteor detections by AMS18 and HUKON, after correction for field-of-view difference.

IMO fireball report webpage (`https://mcse.imo.net`) to collect the observed fireballs over Hungary as reported by visual observers between 2020 and 2023. Multiple detections were filtered out, so each fireball was counted only once. The results are plotted together in Figure 7. It is seen that the two independent datasets are consistent with each other. It confirms the hypothesis that the magnitude distribution of bright fireballs can be modeled with the population index of $r \sim 1.5$, which is significantly less than that of the sporadic meteors. Also, based on the detections by the KoMON system one can predict the true number of very bright fireballs reasonably well.

4.4 Comparison of MetRec-based cameras with AllSky7 units

Since the AllSky7 units provide all-sky coverage, limiting magnitude comparable to that of the MetRec-based cameras and non-stop operation, they are expected to become the next generation of autonomous meteor cameras when the MetRec-based video cameras are retired. Thus, it is useful to compare the performance of the two camera systems in order to test whether the AllSky7 cameras delivered datasets similar to MetRec, both in quantity and quality.

Because the Python-based software of the AllSky7 cameras are still under continuous development (Hankey, personal communication), in this paper we use only the total number of meteors recorded by the AllSky7 stations at our disposal (Table 3) as a test parameter. The meteor numbers were collected from the camera servers by summing up the number of "reduced" meteor events on each night, after visually inspecting all frames and removing the likely artificial records (usually due to airplanes).

In the left panel of Figure 8 we plot the sum of the recorded meteors in each month since the deployment of the individual stations as a function of Julian date. It is seen at first glance that the summed meteor numbers from the different stations are more-or-less consistent with each other, even though the individual stations are distributed at $\sim 100 - 200$ km from each other, thus, they may experience different observing/weather conditions. On the other hand, it is also visible that the monthly meteor numbers show a declining trend for all cameras during the first $\sim$ 800 days after deployment. This decline of the recorded meteor numbers seems to be less pronounced for AMS72 during the 1st year of its operation, but then it also develops the same declining trend in its recorded meteors.

In the right panel of Figure 8 the data from AMS18 are compared with the monthly sum of meteors captured by `HUKON`. These two cameras are both placed at the same site, on the rooftop of the headquarters of Konkoly Observatory in Budapest, Hungary, thus, weather-related differences are not expected. The `HUKON` data were corrected for the smaller field-of-view of the camera, thus, they represent the expected number of meteors as if `HUKON` were an all-sky camera, like AMS18. It is seen that the mean level of the `HUKON` data is relatively constant each year (except, of course, the peak amplitudes due to the different activity levels of the richest meteor showers). On the contrary, the meteor numbers from AMS18 show a notable decline with respect to the `HUKON` data. Since these two cameras are at the same site, this illustrates that the decline is not due to the general and continuous worsening of the observing conditions (e.g. climate change) over Hungary. Instead, it is suspected that this effect is caused by some kind of technical reasons affecting the AllSky7 camera stations.

In Figure 9 we plot the ratio of the monthly meteor numbers from three different AllSky7 station and the nearest MetRec-based cameras. The decline in the AMS18/`HUKON` data is clearly visible, as above. The AMS72/`HUPIS` ratio seems to be more stable, but the second part of the curve (the data taken in 2023) shows wide oscillations preventing the observability of any long-term trend. The AMS98/`HUHOD` ratio spans a shorter range than the other two, but it suggests the same declining trend as the AMS18 data.

Thus, it is concluded that all AllSky7 stations (except maybe AMS72) managed by our group show a general long-term decline in the recorded monthly meteor numbers, while such a decline is not visible in the data of our MetRec-based cameras. According to the developer of the AllSky7 system (Hankey, personal communication), this is software-related due to multiple reasons. One is related to the applied screening criterion:

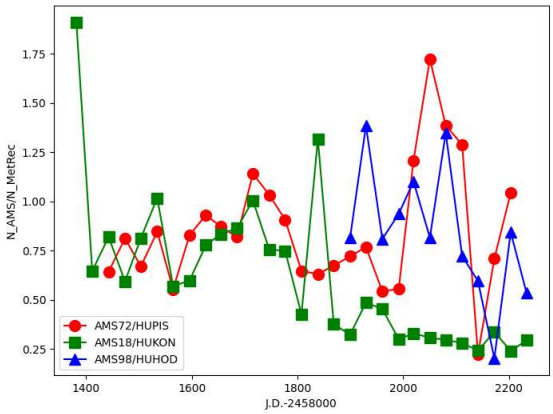

Figure 9 – Ratio of AMS and MetRec meteor numbers.

previously the software was designed to select meteors whose tracks contain at least three measured points, while later it was changed to keep only those that have at least 5 points. Also, sometimes the screening AI unintentionally misses some of the faint and short meteors. Since the AllSky7 system was specifically designed to be triggered by meteors that can be simultaneously measured from many sites, these changes resulted in better performance of the system as a whole. However, our analysis above shows that with the present conditions the data from the individual AllSky7 stations are less suitable for statistical studies than those from the MetRec-based cameras.

5 Conclusion

In this paper we presented a statistical study of the data from three different meteor camera system operating in Hungary from 2020 to 2023. Based on the results detailed in the previous sections, we draw the following conclusions.

1. We measured the population index of all sporadic meteors detected by our MetRec-based cameras, and obtained $\langle r \rangle = 2.85 \pm 0.48$ as the mean value and standard deviation. This is consistent with the results by Jennniskens (1994), Rendtel (2006) and Vida et al. (2020). Unlike Betzler (2023), we did not detect annual variation in the population index of sporadic meteors.

2. The hourly rate of sporadic meteors was estimated based on the data provided by MetRec. We got $\mathrm{HR_{spo}} = 28.4 \pm 8.4$ sporadic meteors/hour for the combined sample from all three cameras (`HUPIS`, `HUKON` and `HUHOD`). This is consistent with the results of Rendtel (2006) based on video meteor data, but seems to be a factor of 3 higher than the estimates by Dubietis and Arlt (2010) from visual observations.

3. The frequency of "fireballs" (defined as meteors brighter than 0 mag in this paper for statistical reasons) was studied by the KoMON camera system. We obtained a monthly rate of $N_{fb} \approx 2.94 \pm 1.91$ events per month. Comparing these data with those from the MetRec-based cameras after scaling those down to 0 limiting magnitude we got reasonable, order-of-magnitude agreement. Note that after applying the brightness correction to -4 mag using a population index of $r \sim 1.5$, we found good agreement with the numbers of true fireballs reported by visual observers from Hungary. This is consistent with the expectations, because most fireballs likely belong to meteor showers, whose population index is substantially lower than that of the sporadic meteors.

4. Comparing the monthly total meteor numbers taken by our AllSky7 stations with similar data from MetRec (after scaling the latter to all-sky) we found an unexpected decrease of the AllSky7 data with respect to those from MetRec. All our AllSky7 stations show the same trend, except maybe AMS72. We tested that it is not related to any long-term worsening of the observing conditions, and it is not likely due to the varying contamination of non-meteor events in the AllSky7 data. All the data suggest that it is probably a software-related reason, which has been confirmed by the developer.

Acknowledgements

This work was supported by the project "Cosmic Effects and Risks" GINOP 2.3.2-15-2016-0003 by the Hungarian National Research Development and Innovation Office, based on funding provided by the European Union.
Special thanks are due to Nagykanizsa Amateur Astronomers Association (especially Zsolt Perkó and Attila Gazdag), and the Bárdos Lajos Primary School, Fehérgyarmat (especially Zoltán Pásztor) for their kind contributions.

References

Betzler A. S. (2023). "The Monthly Rates of TV Sporadic Meteors Between 2014 and 2021". *Earth, Moon, and Planets*, **127:1**, 1.

Campbell-Brown M. D. and Jones J. (2006). "Annual variation of sporadic radar meteor rates". *Monthly Notices of the Royal Astronomical Society*, **367:2**, 709–716.

Dubietis A. and Arlt R. (2010). "Periodic Variability of Visual Sporadic Meteor Rates". *Earth, Moon, and Planets*, **106:2-4**, 105–111.

Howie R. M., Paxman J., Bland P. A., Towner M. C., Sansom E. K., and Devillepoix H. A. R. (2017). "Submillisecond fireball timing using de Bruijn timecodes". *Meteoritics and Planetary Science*, **52:8**, 1669–1682.

Jenniskens P. (1994). "Meteor stream activity I. The annual streams". *Astronomy and Astrophysics*, **287**, 990–1013.

Jones J. and Brown P. (1993). "Sporadic meteor radiant distributions - Orbital survey results". *Monthly Notices of the Royal Astronomical Society*, **265**, 524.

McIntosh B. A. (1991). "Debris from Comets: the Evolution of Meteor Streams". In Newburn, R. L. J., Neugebauer M., and Rahe J., editors, *IAU Colloq. 116: Comets in the post-Halley era*, volume 167 of *Astrophysics and Space Science Library*. page 557.

Molau S. (2015). "Population index reloaded". In *International Meteor Conference Mistelbach, Austria*. page 11.

Rendtel J. (2006). "Visual Sporadic Meteor Rates". *WGN, Journal of the International Meteor Organization*, **34:3**, 71–76.

Vida D., Campbell-Brown M., Brown P. G., Egal A., and Mazur M. J. (2020). "A new method for measuring the meteor mass index: application to the 2018 Draconid meteor shower outburst". *Astronomy and Astrophysics*, **635**, A153.

Wiegert P., Vaubaillon J., and Campbell-Brown M. (2009). "A dynamical model of the sporadic meteoroid complex". *Icarus*, **201:1**, 295–310.

Ye Q. and Jenniskens P. (2022). "Comets and meteor showers". *arXiv e-prints*, page arXiv:2209.10654.

Handling Editor: Javor Kac
This paper has been typeset from a LaTeX file prepared by the authors.

The International Meteor Organization

www.imo.net

Follow us on Facebook InternationalMeteorOrganization

Follow us on Twitter @IMOMeteors

Council

President: Cis Verbeeck,
Bogaertsheide 5, 2560 Kessel, Belgium.
e-mail: cis.verbeeck@gmail.com

Vice-President: Juraj Tóth,
Fac. Math., Phys. & Inf., Comenius Univ.,
Mlynska dolina, 84248 Bratislava, Slovakia.
e-mail: toth@fmph.uniba.sk

Secretary-General: Robert Lunsford,
14884 Quail Valley Way, El Cajon,
CA 92021-2227, USA. tel. +1 619 755 7791
e-mail: lunro.imo.usa@cox.net

Treasurer: Marc Gyssens, Heerbaan 74,
B-2530 Boechout, Belgium.
e-mail: marc.gyssens@uhasselt.be
BIC: GEBABEBB
IBAN: BE30 0014 7327 5911
Bank transfer costs are always at your expense.

Other Council members:
Karl Antier, 16, rue de la République,
F-04100 Manosque, France.
e-mail: karl.antier@gmx.fr
Javor Kac (see details under WGN)
Detlef Koschny, Zeestraat 46,
NL-2211 XH Noordwijkerhout, Netherlands.
e-mail: detlef.koschny@tum.de
Sirko Molau, Abenstalstraße 13b, D-84072
Seysdorf, Germany. e-mail: sirko@molau.de
Francisco Ocaña Gonzalez, C/ Arquitectura, 7.
28005 Madrid, Spain.
e-mail: francisco.ocana.gonzalez@gmail.com
Vincent Perlerin, 16, rue Georges Bernanos,
51100 Reims, France.
e-mail: vperlerin@gmail.com
Jürgen Rendtel, Eschenweg 16, D-14476
Marquardt, Germany. e-mail: jrendtel@aip.de

Commission Directors

Visual Commission: Jürgen Rendtel
Generic e-mail address: visual@imo.net
Electronic visual report form:
http://www.imo.net/visual/report/electronic
Video Commission: Sirko Molau (video@imo.net)
Photographic Commission: Bill Ward
(bill_meteor@yahoo.com)
Generic e-mail address: photo@imo.net
Radio Commission: Chris Steyaert
(radio@imo.net)
Fireball Commission: Robert Lunsford
Online fireball reports:
http://fireballs.imo.net

Webmaster

Karl Antier, e-mail: webmaster@imo.net

WGN

Editor-in-chief: Javor Kac
Na Ajdov hrib 24, SI-2310 Slovenska Bistrica,
Slovenia. e-mail: wgn@imo.net;
include METEOR in the e-mail subject line

Editorial board: Ž. Andreić, D.J. Asher,
F. Bettonvil, M. Gyssens, C. Hergenrother,
T. Heywood, J. Rendtel, C. Verbeeck,
S. de Vet, D. Vida.

IMO Sales

Available from the Treasurer or the Electronic Shop on the IMO Website	€	$
IMO membership, including subscription to WGN Vol. 51 (2023)		
Surface mail	26	30
Air Mail (outside Europe only)	49	56
Electronic subscription only	21	24
Proceedings of the International Meteor Conference on paper		
1990, 1991, 1995, 1996, 1999, 2000, 2002, 2003, per year	9	12
2007, 2010, 2011, per year	15	20
2012, 2013, 2015, 2017 per year	25	32
Proceedings of the Meteor Orbit Determination Workshop 2006	15	20
Radio Meteor School Proceedings 2005	15	20
Handbook for Meteor Observers	23	29
Meteor Shower Workbook	12	16
Electronic media		
Meteor Beliefs Project ZIP archive	6	8

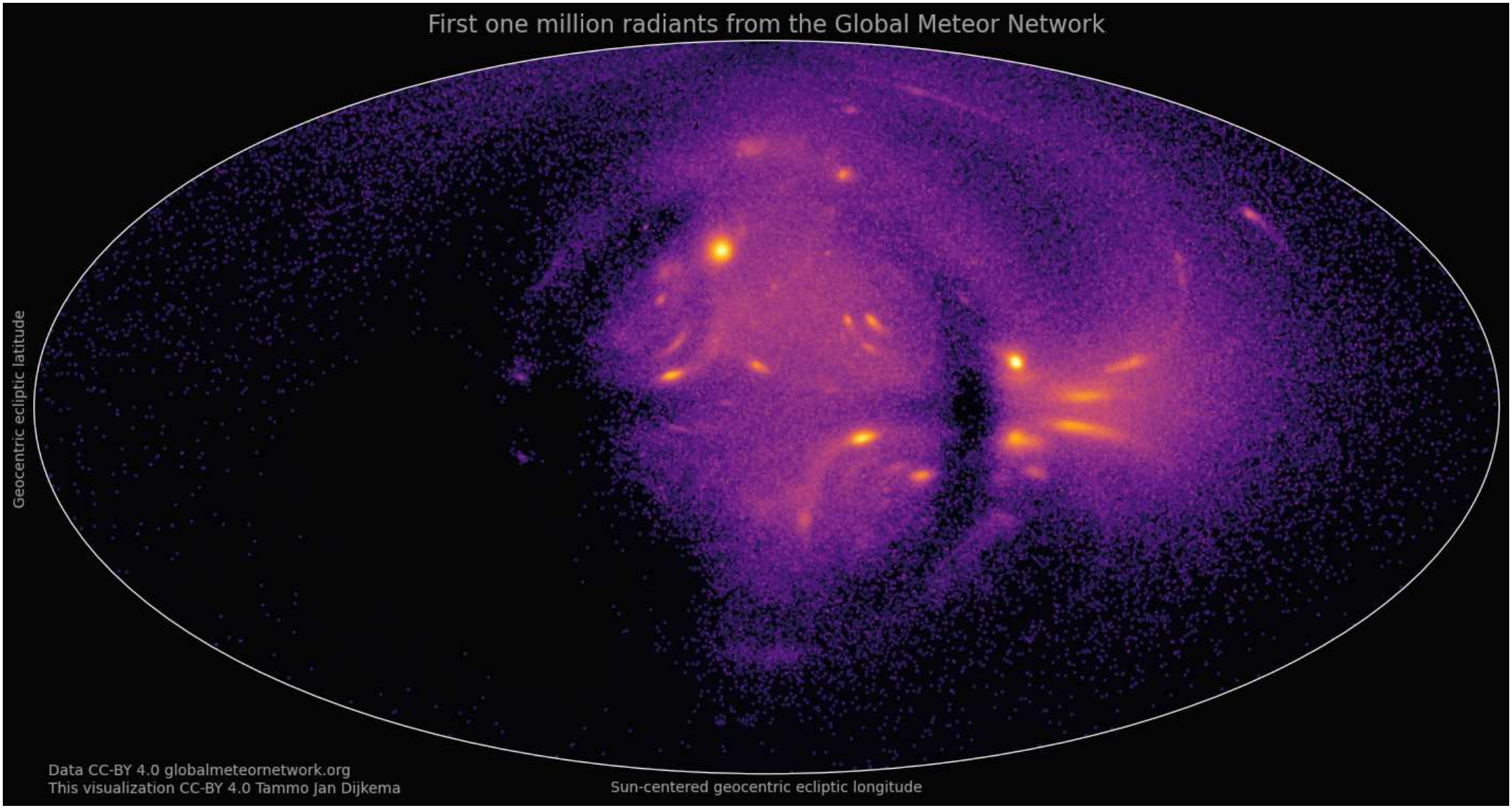
First one million radiants from the Global Meteor Network
Geocentric ecliptic latitude
Sun-centered geocentric ecliptic longitude
Data CC-BY 4.0 globalmeteornetwork.org
This visualization CC-BY 4.0 Tammo Jan Dijkema